



# **Visible Infrared Imaging Radiometer Suite (VIIRS) Land Surface Temperature and Emissivity Product Collection 1 Algorithm Theoretical Basis Document**

*Glynn Hulley, Tanvir Islam, Robert Freepartner, Nabin Malakar*

*Jet Propulsion Laboratory, California Institute of Technology*

**National Aeronautics and  
Space Administration  
Jet Propulsion Laboratory  
California Institute of Technology  
Pasadena, California**

**December 2016**

---

This research was carried out at the Jet Propulsion Laboratory, California Institute of Technology, under a contract with the National Aeronautics and Space Administration.

Reference herein to any specific commercial product, process, or service by trade name, trademark, manufacturer, or otherwise, does not constitute or imply its endorsement by the United States Government or the Jet Propulsion Laboratory, California Institute of Technology.

© 2016. California Institute of Technology. Government sponsorship acknowledged.

## Change History Log

Revision	Effective Date	Prepared by	Description of Changes
Draft	09/01/2015	Glynn Hulley	First Draft based on MOD21 ATBD
Draft	01/03/2016	Tanvir Islam, Glynn Hulley	Updated Atmospheric Correction and WVS Method Sections
Draft	12/06/2016	Glynn Hulley	Updated with MODIS/VIIRS continuity and most recent validation results

## Contacts

Readers seeking additional information about this study may contact the following:

**Glynn C. Hulley (PI)**

MS 183-509

Jet Propulsion Laboratory

4800 Oak Grove Dr.

Pasadena, CA 91109

Email: [glynn.hulley@jpl.nasa.gov](mailto:glynn.hulley@jpl.nasa.gov)

Office: (818) 354-2979

# Contents

<b>1</b>	<b>Introduction .....</b>	<b>6</b>
1.1	Rationale for the Product.....	6
1.2	Intended User Community .....	8
1.2.1	Use of LST&E in Climate/Ecosystem Models .....	8
1.2.2	Use of LST&E in Cryospheric Research .....	10
1.2.3	Use of LST&E in Atmospheric Retrieval Schemes.....	11
<b>2</b>	<b>The Algorithm .....</b>	<b>11</b>
2.1	Technical Background and Heritage .....	11
2.2	Algorithm Description.....	13
2.2.1	Atmospheric Correction.....	13
2.2.2	Water Vapor Scaling Method .....	20
2.2.3	TES Algorithm.....	25
<b>3</b>	<b>VIIRS and MODIS LST&amp;E continuity .....</b>	<b>35</b>
<b>4</b>	<b>Validation and Product Accuracy .....</b>	<b>41</b>
4.1	Water Sites .....	42
4.2	Vegetated Sites.....	44
4.3	Pseudo-invariant Sand Dune Sites.....	45
4.3.1	Emissivity Validation .....	45
4.3.2	Emissivity comparison with ASTER GED.....	47
4.3.3	LST Validation .....	50
<b>5</b>	<b>Data Formats .....</b>	<b>54</b>
5.1	Format .....	54
5.2	QA Metadata .....	55
<b>6</b>	<b>References .....</b>	<b>58</b>

## Figures

Figure 1. Simulated atmospheric transmittance for a US Standard Atmosphere (red) and tropical atmosphere (blue) in the 3–12 $\mu\text{m}$ region. Also shown is the solar irradiance contribution $\text{W}/\text{m}^2/\mu\text{m}^2$ .....	14
Figure 2. Radiance simulations of the surface-emitted radiance, surface-emitted and reflected radiance, and at-sensor radiance using the MODTRAN 5.2 radiative transfer code, US Standard Atmosphere, quartz emissivity spectrum, surface temperature = 300 K, and viewing angle set to nadir. Vertical bars show placements of the VIIRS TIR bands M14 (~8.55 $\mu\text{m}$ ), M15 (~11 $\mu\text{m}$ ), and M16 (~12 $\mu\text{m}$ ).....	15
Figure 3. VIIRS spectral response functions for bands M14 (blue), M15 (red), and M16 (yellow).....	16
Figure 4. WVS factor $\gamma$ computed for a VIIRS scene on 13 January 2014. The image has been interpolated and smoothed.....	21
Figure 5. TPW Vs Skin Temperature plot showing the wide distribution of input profiles.....	24
Figure 6. Global SeeBor database showing station locations for day and night sondes.....	24
Figure 7. Flow diagram showing all steps in the retrieval process in generating the VIIRS VNP21 LST&E product starting with TIR at-sensor radiances and progressing through atmospheric correction, cloud detection, and the TES algorithm.....	27
Figure 8. Flow diagram of the TES algorithm in its entirety, including the NEM, RATIO, and MMD modules. Details are included in the text, including information about the refinement of <i>emax</i> .....	28
Figure 9. VIIRS calibration curve of minimum emissivity vs. MMD. The lab data (crosses) are computed from 150 spectra consisting of a broad range of terrestrial materials (rocks, sand, soil, water, vegetation, and ice). 32	32
Figure 10. Clockwise from top left: VIIRS land surface emissivity for band M14 (8.55 $\mu\text{m}$ ); band M15 (10.76 $\mu\text{m}$ ), surface temperature (K) and band M15 emissivity (12 $\mu\text{m}$ ); output from the TES algorithm over northeast Africa on 13 January 2014.....	33
Figure 11. Differences between the VIIRS and MODIS LST products in K using the TES algorithm (top left) and the split-window algorithm (top right). Corresponding VIIRS LST (bottom left) and MERRA-2 precipitable water vapor in cm (bottom right) are also shown. The granule overpass is on 11 August 2012 UTC 2040.....	37
Figure 12. (Top) Histogram demonstrating the differences between VIIRS and MODIS LST products for all observations over continental USA (CONUS) during Jan, Feb, Aug, and Sep 2012 for two different algorithms: TES and split-window. The TES algorithm is currently used to produce the NASA LST&E products for MODIS and VIIRS (MOD21 and VNP21), while the split-window algorithm is used in the to produce the heritage MOD11 product(s) and the NOAA VLST product. (Bottom) same as above except only data for summer time (Aug, Sep).....	38
Figure 13. VIIRS minus MODIS LST RMSE for the split-window algorithms (top) and TES algorithm (bottom) calculated from 4 months of MODIS and VIIRS SNO's over CONUS during Jan, Feb, Aug, and Sep 2012. LST differences were grouped according to standard IGBP classification. Note large differences in the split-window results especially for arid and semi-arid classes (shrublands, bare), while TES results are consistent and less than 1 K across all cover types. ....	39
Figure 14. LST differences between MODIS and VIIRS vs total column water vapor and LST for the split-window algorithms (top), and TES algorithm (bottom). Differences in formulation, coefficient generation, and emissivity assignment result in large differences between the current MODIS and VIIRS split-window LST products. ....	40
Figure 15. Emissivity spectra comparisons on June 15, 2000 over the Salton Sea between ASTER (3-band), ASTER (5-band), and MODTES, using the TES algorithm along with lab spectra of water from the ASTER spectral library. Results from the WVS method and the STD atmospheric correction are also shown. An estimate of the PWV from the MOD07 atmospheric product indicates very high humidity on this day.....	43
Figure 16. Scatterplot of VNP21 retrieved LST vs JPL radiometer LST at the inland water validation sites.....	44
Figure 17. Laboratory-measured emissivity spectra of sand samples collected at ten pseudo-invariant sand dune validation sites in the southwestern United States. The sites cover a wide range of emissivities in the TIR region.....	46
Figure 18. The emissivity maps from the VNP21 retrieval (top left) and the ASTER GED (top right) at the VIIRS band M14 (8.55 $\mu\text{m}$ ). Corresponding emissivity difference map (bottom left) and the histogram of their differences (bottom right) are also shown. The ASTER GED emissivity is adjusted to the VIIRS M14 band (~8.55 $\mu\text{m}$ ) for comparison. The granule overpass is on 19 June 2014 UTC 2050.....	49

Figure 19. Emissivity spectra comparison between VNP21 retrieved emissivity and the ASTER GED v3 emissivities that were spectrally and spatially adjusted to match VIIRS at 4 pseudo-invariant sand dune sites.....50

Figure 20. An example of the R-based LST validation method applied to the VNP21 (VTES) and NOAA VLST LST products over 3 pseudo-invariant sand dune sites (Algodones, Kelso, Little Sahara) and two vegetated sites (Redwood, Texas Grass) using all data during 2012. NCEP profiles and lab-measured emissivities from samples collected at the sites were used for the R-based calculations .....54

## Tables

Table 1: Geophysical data available in the MERRA-2 reanalysis product. Columns under Mandatory specify if the variables is needed for determining atmospheric correction parameters. Data are output in 6hr analysis for 42 pressure levels at 1/2 degree x 2/3 degree spatial resolution (longitude=576, latitude=361) .....	19
Table 2. VIIRS band model parameters in equation (6) .....	24
Table 3. The core set of global validation sites according to IGBP class to be used for validation and calibration of the VIIRS VNP21 land surface temperature and emissivity product. ....	42
Table 4. R-based LST validation statistics from three pseudo-invariant sand dune sites and two vegetated sites using all VNP21 and VLST LST retrievals from 2012-2015. ....	52
Table 5. The Scientific Data Sets (SDSs) in the VNP21 product .....	54
Table 6. Bit flags defined in the QC_Day and QC_Night SDS in the VNP21A2 product. (Note: Bit 0 is the least significant bit). ....	56

# 1 Introduction

This document outlines the theory and methodology for generating the Visible Infrared Imaging Radiometer Suite (VIIRS) Level-2 VNP21 1-km land surface temperature and emissivity (LST&E) product using the Temperature Emissivity Separation (TES) algorithm. The VNP21 product, will include the LST and emissivity for three VIIRS thermal infrared (TIR) bands M14 (8.55 micron), M15 (10.76 micron), and M16 (12 micron), and will be generated for data from the Suomi National Polar-orbiting Partnership (Suomi-NPP) and Joint Polar Satellite System (JPSS) platforms. This is version 1.0 of the ATBD and the goal is to maintain a ‘living’ version of this document with changes made when necessary.

## 1.1 Rationale for the Product

Land Surface Temperature and Emissivity (LST&E) data are critical variables for studying a wide variety of Earth surface processes and surface-atmosphere interactions such as evapotranspiration, land cover dynamics, and in water vapor retrieval schemes. LST&E have been identified as an important Earth System Data Record (ESDR) by NASA and many other international organizations (NASA Strategic Roadmap Committee #9, 2005; European Space Agency (ESA); Global Climate Observing System (GCOS), 2003; Climate Change Science Program (CCSP), 2006; IPCC, 2007; and the EarthTemp network (Merchant 2012).

The land surface temperature and emissivity (LST&E) are derived from the surface radiance that is obtained by atmospherically correcting the at-sensor radiance. LST&E data are used for many Earth surface related studies such as surface energy balance modeling (Zhou et al. 2003b) and land-cover land-use change detection (French et al. 2008), while they are also critical for accurately retrieving important climate variables such as air temperature and relative humidity (Yao et al. 2011). The LST is an important long-term climate indicator, and a key variable for drought monitoring over arid lands (Anderson et al. 2011a; Rhee et al. 2010). The LST is an input to ecological models that determine important variables used for water use management such as evapotranspiration and soil moisture (Anderson et al. 2011b). Multispectral emissivity retrievals are also important for Earth surface studies. For example, emissivity spectral signatures are important for geologic studies and mineral mapping studies (Hook et al. 2005; Vaughan et al. 2005). This is because emissivity features in the TIR region are unique for many different types of materials that make up the Earth’s surface, such as quartz, which is ubiquitous in most of the arid



regions of the world. Emissivities are also used for land use and land cover change mapping since vegetation fractions can often be inferred if the background soil is observable (French et al. 2008). Accurate knowledge of the surface emissivity is critical for accurately recovering the LST, especially over land where emissivity variations can be large both spectrally and spatially.

Both LST&E determine the total amount of longwave radiation emitted from the Earth's surface, and are therefore key variables in many energy balance models that estimate important surface biophysical variables such as evapotranspiration and plant-available soil moisture (Anderson et al. 2007; Moran 2003) that are ingested into drought monitoring systems such as the U.S. The National Integrated Drought Information System (NIDIS). LST&E data are also essential for balancing the Earth's surface radiation budget; for example an error of 0.1 in the emissivity will result in climate models having errors of up to  $7 \text{ Wm}^{-2}$  in their upward longwave radiation estimates—a much larger term than the surface radiative forcing due to an increase in greenhouse gases ( $\sim 2\text{-}3 \text{ Wm}^{-2}$ ) (Zhou et al. 2003b). LST&E are also utilized in monitoring land-cover / land-use changes (French and Inamdar 2010; French et al. 2008), and in retrieving important climate variables such as air temperature and water vapor in atmospheric retrieval schemes (Seemann et al. 2003; Yao et al. 2011).

Since the equation for retrieving LST&E is underdetermined, multiple retrieval methods have been developed that are optimized for a particular set of conditions. The simplest and efficient of these retrieval methods is the split-window (SW) algorithm, which is used to generate the heritage MODIS LST&E products (MOD/MYD11) and the current VIIRS LST Environmental Data Record (EDR). In the SW approach, emissivities are assigned according to a land classification scheme (Snyder et al. 1998), and atmospheric effects are compensated for by using the differential absorption features from two longwave window bands (11-12  $\mu\text{m}$ ). This approach has been used with much success over oceans to compute sea surface temperatures, and works well over densely vegetated areas and water where the assumption of single fixed emissivity is valid (Coll et al. 2009a). However, cold biases of 3-5 K are often found over semi-arid and arid regions because these regions have much higher emissivity variability (Hulley and Hook 2009a), and only one fixed emissivity from the 'barren' land class is assigned to these regions in the split-window approach. Recent validation of the VIIRS LST EDR product with ground-based measurements showed good accuracy over vegetated and water targets, but large cold biases of up to 5 K over arid targets. Performance is further degraded for high atmospheric water vapor content

conditions where differences up to 15 K have been observed with the MYD11 heritage LST products. A further shortcoming in the current VIIRS LST algorithm is that the operational product does not produce a dynamically retrieved land surface emissivity product similar to the current MODIS MOD11B1 and MOD21 products, and the additional information from the VIIRS M14 (8.5  $\mu\text{m}$ ) thermal infrared band is not utilized in the LST retrieval scheme.

The second retrieval method is the physics-based Temperature Emissivity Separation (TES) algorithm, which uses an emissivity model based on the variability in the surface radiance data to dynamically retrieve both LST and spectral emissivity (Gillespie et al. 1998). This approach is used to generate the ASTER standard products (AST05, AST08), and also the MODIS MOD21 product (to be released with Collection 6). The TES algorithm has consistent accuracy over all land cover types when combined with a Water Vapor Scaling (WVS) model and dynamically retrieves the spectral emissivity (bands 29, 31, and 32 for MODIS) at 1-km resolution. We will develop a VIIRS LST&E product based on the TES approach - VNP21.

Several studies over the past decade have shown that the split-window and TES approaches are complementary, with the split-window approach being more stable over heavily vegetated regions and the physics-based TES approach working better over semi-arid and arid regions (Gottsche and Hulley 2012; Hulley and Hook 2009a; Hulley et al. 2010). By taking advantage of this fact, we will also develop a unified VIIRS LST product using a combination of the well-established and complementary TES and split-window algorithms (similar to MOD11/MOD21 approaches).

## **1.2 Intended User Community**

LST&E are key variables for explaining the biophysical processes that govern the balances of water and energy at the land surface. LST&E data are used in many research areas including ecosystem models, climate models, cryospheric research, and atmospheric retrieval schemes. Our team has been carefully selected to include expertise in these areas. The descriptions below summarize how LST&E data are typically used in these areas.

### *1.2.1 Use of LST&E in Climate/Ecosystem Models*

Emissivity is a critical parameter in climate models that determine how much thermal radiation is emitted back to the atmosphere and space and therefore is needed in surface radiation budget calculations, and also to calculate important climate variables such as LST (e.g., Jin and

Liang 2006; Zhou et al. 2003b). Current climate models represent the land surface emissivity by either a constant value or very simple parameterizations due to the limited amount of suitable data. Land surface emissivity is prescribed to be unity in the Global Climate Models (GCMs) of the Center for Ocean-Land-Atmosphere Studies (COLA) (Kinter et al. 1988), the Chinese Institute of Atmospheric Physics (IAP) (Zeng et al. 1989), and the US National Meteorological Center (NMC) Medium-Range Forecast (MRF). In the recently developed NCAR Community Land Model (CLM3) and its various earlier versions (Bonan et al. 2002; Oleson et al. 2004), the emissivity is set as 0.97 for snow, lakes, and glaciers, 0.96 for soil and wetlands, and vegetation is assumed to be black body. For a broadband emissivity to correctly reproduce surface energy balance statistics, it needs to be weighted both over the spectral surface blackbody radiation and over the downward spectral sky radiances and used either as a single value or a separate value for each of these terms. This weighting depends on the local surface temperatures and atmospheric composition and temperature. Most simply, as the window region dominates the determination of the appropriate single broadband emissivity, an average of emissivities over the window region may suffice.

Climate models use emissivity to determine the net radiative heating of the canopy and underlying soil and the upward (emitted and reflected) thermal radiation delivered to the atmosphere. The oversimplified representations of emissivity currently used in most models introduce significant errors in the simulations of climate. Unlike what has been included in climate models up to now, satellite observations indicate large spatial and temporal variations in land surface emissivity with surface type, vegetation amount, and soil moisture, especially over deserts and semi-deserts (Ogawa 2004; Ogawa et al. 2003). This variability of emissivity can be constructed by the appropriate combination of soil and vegetation components.

Sensitivity tests indicate that models can have an error of 5–20  $\text{Wm}^{-2}$  in their surface energy budget for arid and semi-arid regions due to their inadequate treatment of emissivity (Jin and Liang 2006; Zhou et al. 2003b), a much larger term than the surface radiative forcing from greenhouse gases. The provision, through this proposal, of information on emissivity with global spatial sampling will be used for optimal estimation of climate model parameters. A climate model, in principle, constructs emissivity at each model grid square from four pieces of information: a) the emissivity of the underlying soil; b) the emissivity of the surfaces of vegetation (leaves and stems); c) the fraction of the surface that is covered by vegetation; and d) the description of the areas and spatial distribution of the surfaces of vegetation needed to determine what fraction of surface

emission will penetrate the canopy. Previously, we have not been able to realistically address these factors because of lack of suitable data. The emissivity datasets developed for this project will be analyzed with optimal estimation theory that uses the spatial and temporal variations of the emissivity data over soil and vegetation to constrain more realistic emissivity schemes for climate models. In doing so, land surface emissivity can be linked to other climate model parameters such as fractional vegetation cover, leaf area index, snow cover, soil moisture, and soil albedo, as explored in Zhou et al. (2003a). The use of more realistic emissivity values will greatly improve climate simulations over sparsely vegetated regions as previously demonstrated by various sensitivity tests (e.g., Jin and Liang 2006; Zhou et al. 2003b). In particular, both daily mean and day-to-night temperature ranges are substantially impacted by the model's treatment of emissivity.

### *1.2.2 Use of LST&E in Cryospheric Research*

Surface temperature is a sensitive energy-balance parameter that controls melt and energy exchange between the surface and the atmosphere. Surface temperature is also used to monitor melt zones on glaciers and can be related to the glacier facies of (Benson 1996), and thus to glacier or ice sheet mass balance (Hall et al. 2006). Analysis of the surface temperature of the Greenland Ice Sheet and the ice caps on Greenland provides a method to study trends in surface temperature as a surrogate for, and enhancement of, air-temperature records, over a period of decades (Comiso 2006). Maps of LST of the Greenland Ice Sheet have been developed using the MODIS 1-km LST standard product, and trends in mean LST have been measured (Hall et al. 2008). Much attention has been paid recently to the warming of the Arctic in the context of global warming. Comiso (2006) shows that the Arctic region, as a whole, has been warming at a rate of  $0.72 \pm 0.10^\circ\text{C}$  per decade from 1981–2005 inside the Arctic Circle, though the warming pattern is not uniform. Furthermore, various researchers have shown a steady decline in the extent of the Northern Hemisphere sea ice, both the total extent and the extent of the perennial or multiyear ice (Parkinson et al. 1999). Increased melt of the margins of the Greenland Ice Sheet has also been reported (Abdalati and Steffen 2001).

Climate models predict enhanced Arctic warming but they differ in their calculations of the magnitude of that warming. The only way to get a comprehensive measurement of surface-temperature conditions over the Polar Regions is through satellite remote sensing. Yet errors in the most surface temperature algorithms have not been well-established. Limitations include the

assumed emissivity, effect of cloud cover, and calibration consistency of the longer-term satellite record.

Comparisons of LST products over snow and ice features reveal LST differences in homogeneous areas of the Greenland Ice Sheet of  $>2^{\circ}\text{C}$  under some circumstances. Because there are many areas that are within a few degrees of  $0^{\circ}\text{C}$ , such as the ice-sheet margin in southern Greenland, it is of critical importance to be able to measure surface temperature from satellites accurately. Ice for which the mean annual temperature is near the freezing point is highly vulnerable to rapid melt.

### *1.2.3 Use of LST&E in Atmospheric Retrieval Schemes*

The atmospheric constituent retrieval community and numerical weather prediction operational centers are expected to benefit from the development of a unified land surface emissivity product. The retrieval of vertical profiles of air temperature and water vapor mixing ratio in the atmospheric boundary layer over land is sensitive to the assumptions used about the infrared emission and reflection from the surface. Even the retrieval of clouds and aerosols over land using infrared channels is complicated by uncertainties in the spectral dependence of the land surface emission. Moreover, weather models improve their estimates of atmospheric temperature and composition by comparisons between observed and model calculated spectral radiances, using an appropriate data assimilation (1D-Var) framework. The model generates forward calculation of radiances by use of their current best estimate of temperature profiles, atmospheric composition, and surface temperature and emissivity. If good prior estimates of infrared emissivity can be provided along with their error characterization, what would otherwise be a major source of error and bias in the use of the satellite radiances in data assimilation can be minimized.

## **2 The Algorithm**

### **2.1 Technical Background and Heritage**

The VNP21 algorithm derives its heritage from the ASTER TES algorithm (Gillespie et al. 1998) and the MODIS MOD21 algorithm (Hulley et al. 2012). ASTER is a five-channel multispectral TIR scanner that was launched on NASA's Terra spacecraft in December 1999 with a 90-m spatial resolution and revisit time of 16 days. The VNP21 LST&E products will be produced globally over all land cover types, excluding open oceans for all cloud-free pixels. It is

anticipated that the Level-2 products will be merged to produce weekly, monthly, and seasonal products, with the monthly product most likely producing global coverage, depending on cloud coverage. The generation of the higher level merged products will be considered a project activity. The VNP21 Level 2 products will be initially inter-compared with the standard VLST products to identify regions and conditions for divergence between the products, and validation will be accomplished using a combination of temperature-based (T-based) and radiance-based (R-based) methods over dedicated field sites.

Maximum radiometric emission for the typical range of Earth surface temperatures, excluding fires and volcanoes, is found in two infrared spectral “window” regions: the midwave infrared (3.5–5  $\mu\text{m}$ ) and the thermal infrared (8–13  $\mu\text{m}$ ). The radiation emitted in these windows for a given wavelength is a function of both temperature and emissivity. Determining the separate contribution from each component in a radiometric measurement is an ill-posed problem since there will always be more unknowns— $N$  emissivities and a single temperature—than the number of measurements,  $N$ , available. For VIIRS, we will be solving for one temperature and three emissivities (VIIRS TIR bands M14, M15, and M16). To solve the ill-posed problem, an additional constraint is needed, independent of the data. There have been numerous theories and approaches over the past two decades to solve for this extra degree of freedom. For example, the ASTER Temperature Emissivity Working Group (TEWG) analyzed ten different algorithms for solving the problem (Gillespie et al. 1999). Most of these relied on a radiative transfer model to correct at-sensor radiance to surface radiance and an emissivity model to separate temperature and emissivity. Other approaches include the SW algorithm, which extends the sea-surface temperature (SST) SW approach to land surfaces, assuming that land emissivities in the window region (10.5–12  $\mu\text{m}$ ) are stable and well known. However, this assumption leads to unreasonably large errors over barren regions where emissivities have large variations both spatially and spectrally. The ASTER TEWG finally decided on a hybrid algorithm, termed the TES algorithm, which capitalizes on the strengths of previous algorithms with additional features (Gillespie et al. 1998).

TES is applied to the land-leaving TIR radiances that are estimated by atmospherically correcting the at-sensor radiance on a pixel-by-pixel basis using a radiative transfer model. TES uses an empirical relationship to predict the minimum emissivity that would be observed from a given spectral contrast, or minimum-maximum difference (MMD) (Kealy and Hook 1993; Matsunaga 1994). The empirical relationship is referred to as the calibration curve and is derived

from a subset of spectra in the ASTER spectral library (Baldrige et al. 2009). A VIIRS calibration curve, applicable to VIIRS TIR bands M14, M15, and M16 is computed. Numerical simulations have shown that TES is able to recover temperatures within 1.5 K and emissivities within 0.015 for a wide range of surfaces and is a well-established physical algorithm that produces seamless images with no artificial discontinuities such as might be seen in a land classification type algorithm (Gillespie et al. 1998).

## 2.2 Algorithm Description

### 2.2.1 Atmospheric Correction

#### 2.2.1.1 Thermal Infrared Radiance

The at-sensor measured radiance in the TIR spectral region (7–14  $\mu\text{m}$ ) is a combination of three primary terms: the Earth-emitted radiance, reflected downwelling sky irradiance, and atmospheric path radiance. The Earth-emitted radiance is a function of temperature and emissivity and gets attenuated by the atmosphere on its path to the satellite. The atmosphere also emits radiation, some of which reaches the sensor directly as “path radiance,” while some gets radiated to the surface (irradiance) and reflected back to the sensor, commonly known as the reflected downwelling sky irradiance. Reflected solar radiation in the TIR region is negligible (Figure 1) and a much smaller component than the surface-emitted radiance. One effect of the sky irradiance is the reduction of the spectral contrast of the emitted radiance, due to Kirchhoff’s law. Assuming the spectral variation in emissivity is small (Lambertian assumption), and using Kirchhoff’s law to express the hemispherical-directional reflectance as directional emissivity ( $\rho_\lambda = 1 - \epsilon_\lambda$ ), the clear-sky at-sensor radiance can be written as three terms: the Earth-emitted radiance described by Planck’s function and reduced by the emissivity factor,  $\epsilon_\lambda$ ; the reflected downwelling irradiance; and the path radiance.

$$L_\lambda(\theta) = [\epsilon_\lambda B_\lambda(T_s) + (1 - \epsilon_\lambda)L_\lambda^\downarrow] \tau_\lambda(\theta) + L_\lambda^\uparrow(\theta) \quad (1)$$

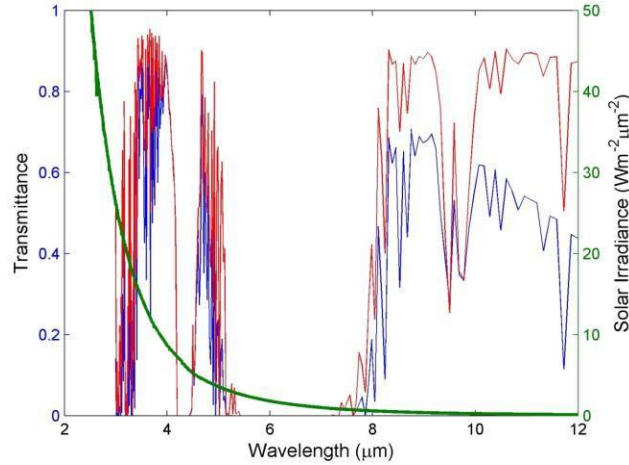


**Figure 1. Simulated atmospheric transmittance for a US Standard Atmosphere (red) and tropical atmosphere (blue) in the 3–12 μm region. Also shown is the solar irradiance contribution  $W/m^2/\mu m^2$ .**

Where:

$L_\lambda(\theta)$  = at-sensor radiance;

$\lambda$  = wavelength;

$\theta$  = observation angle;

$\epsilon_\lambda$  = surface emissivity;

$T_s$  = surface temperature;

$L_\lambda^\downarrow$  = downwelling sky irradiance;

$\tau_\lambda(\theta)$  = atmospheric transmittance;

$L_\lambda^\uparrow(\theta)$  = atmospheric path radiance

$B_\lambda(T_s)$  = Planck function, described by Planck's law:

$$B_\lambda = \frac{c_1}{\pi\lambda^5} \left( \frac{1}{\exp\left(\frac{c_2}{\lambda T}\right) - 1} \right) \quad (2)$$

$c_1 = 2\pi h c^2 = 3.74 \cdot 10^{-16} \text{ W}\cdot\text{m}^2$  (1<sup>st</sup> radiation constant)

$h = 6.63 \cdot 10^{-34} \text{ W}\cdot\text{s}^2$  (Planck's constant)

$c_2 = h \cdot c / k = 1.44 \times 10^4 \text{ }\mu\text{m}\cdot\text{K}$  (2<sup>nd</sup> radiation constant)

$k = 1.38 \times 10^{-23} \text{ W}\cdot\text{s}\cdot\text{K}^{-1}$  (Boltzmann's constant)

$c = 2.99 \cdot 10^8 \text{ m}\cdot\text{s}^{-1}$  (speed of light)



Figure 2 shows the relative contributions from the surface-emission term, surface radiance, and at-sensor radiance for a US Standard Atmosphere, quartz emissivity spectrum, and surface temperature set to 300 K. Vertical bars show the center placement of the three VIIRS TIR bands M14 (~8.55  $\mu\text{m}$ ), M15 (~11  $\mu\text{m}$ ), and M16 (~12  $\mu\text{m}$ ). The reflected downwelling term adds a small contribution in the window regions but will become more significant for more humid atmospheres. The at-sensor radiance shows large departures from the surface radiance in regions where atmospheric absorption from gases such as  $\text{CO}_2$ ,  $\text{H}_2\text{O}$ , and  $\text{O}_3$  are high.

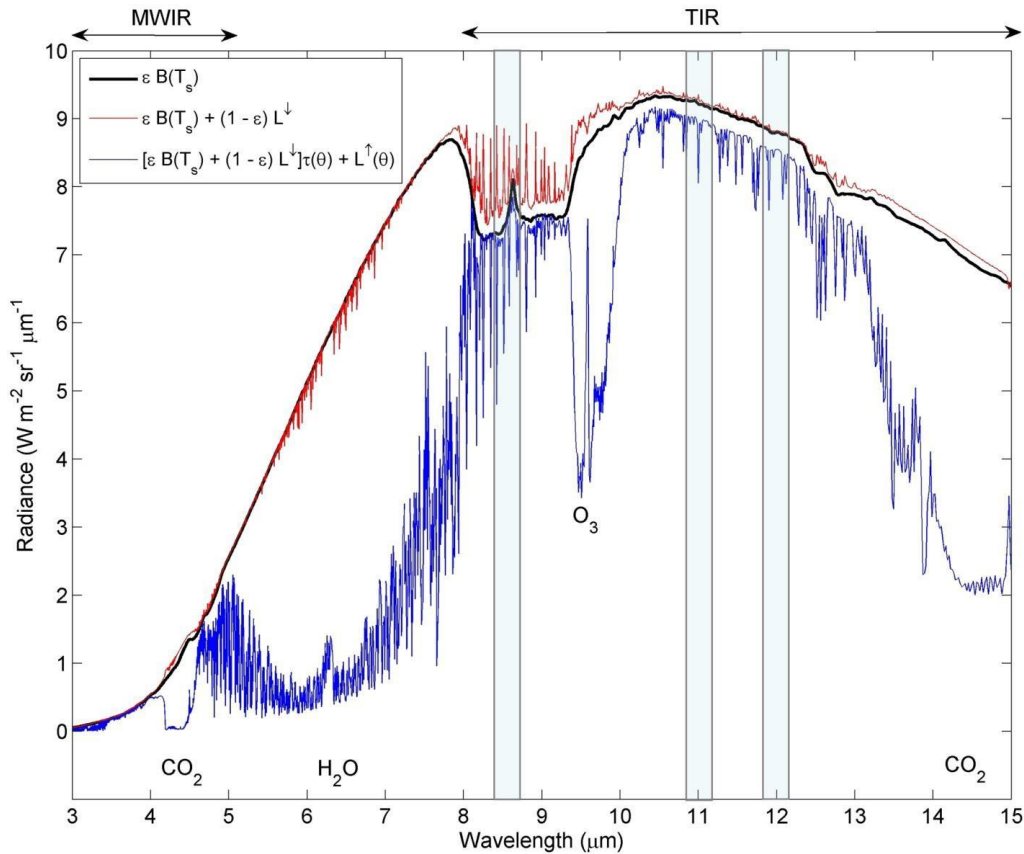


**Figure 2. Radiance simulations of the surface-emitted radiance, surface-emitted and reflected radiance, and at-sensor radiance using the MODTRAN 5.2 radiative transfer code, US Standard Atmosphere, quartz emissivity spectrum, surface temperature = 300 K, and viewing angle set to nadir. Vertical bars show placements of the VIIRS TIR bands M14 (~8.55  $\mu\text{m}$ ), M15 (~11  $\mu\text{m}$ ), and M16 (~12  $\mu\text{m}$ ).**

Equation (1) gives the at-sensor radiance for a single wavelength,  $\lambda$ , while the measurement from a sensor is typically measured over a range of wavelengths, or band. The at-sensor radiance for a discrete band,  $i$ , is obtained by weighting and normalizing the at-sensor spectral radiance

calculated by equation (1) with the sensor's spectral response function for each band,  $Sr_\lambda$ , as follows:

$$L_i(\theta) = \frac{\int Sr_\lambda(i) \cdot L_\lambda(\theta) \cdot d\lambda}{Sr_\lambda(i) \cdot d\lambda} \quad (3)$$

Using equations (1) and (2), the surface radiance for band  $i$  can be written as a combination of two terms: Earth-emitted radiance, and reflected downward irradiance from the sky and surroundings:

$$L_{s,i} = \epsilon_i B_i(T_s) + (1 - \epsilon_i) L_i^\downarrow = \frac{L_i(\theta) - L_i^\uparrow(\theta)}{\tau_i(\theta)} \quad (4)$$

The atmospheric parameters,  $L_\lambda^\downarrow$ ,  $\tau_\lambda(\theta)$ ,  $L_\lambda^\uparrow(\theta)$ , are estimated with a radiative transfer model such as RTTOV discussed in the next section, using input atmospheric fields of air temperature, relative humidity, and geopotential height. Figure 3 shows VIIRS spectral response functions for bands M14, M15 and M16 plotted for a mid-latitude summer atmosphere.

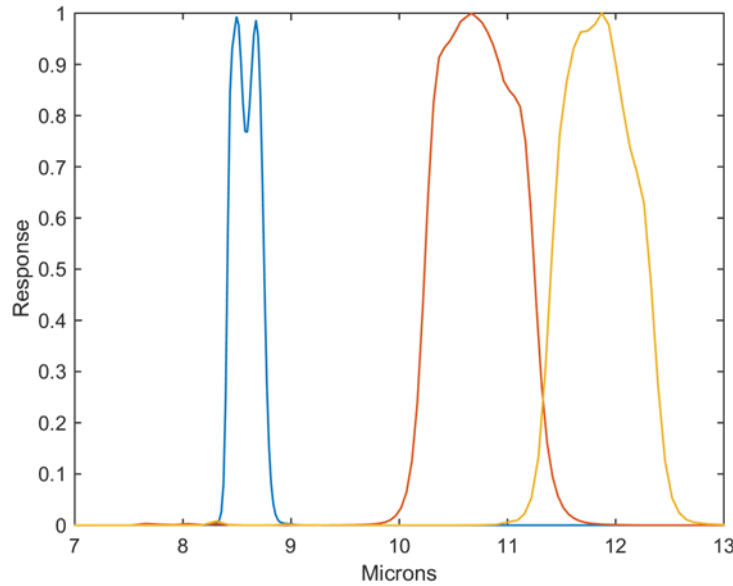


Figure 3. VIIRS spectral response functions for bands M14 (blue), M15 (red), and M16 (yellow).

### 2.2.1.2 Emissivity

The emissivity of an isothermal, homogeneous emitter is defined as the ratio of the actual emitted radiance to the radiance emitted from a black body at the same thermodynamic temperature (Norman and Becker 1995),  $\epsilon_\lambda = R_\lambda / B_\lambda$ . The emissivity is an intrinsic property of the Earth's surface and is an independent measurement of the surface temperature, which varies with

irradiance and local atmospheric conditions. The emissivity of most natural Earth surfaces for the TIR wavelength ranges between 8 and 12  $\mu\text{m}$  and, for a sensor with spatial scales  $<100$  m, varies from  $\sim 0.7$  to close to 1.0. Narrowband emissivities less than 0.85 are typical for most desert and semi-arid areas due to the strong quartz absorption feature (reststrahlen band) between the 8- and 9.5- $\mu\text{m}$  range, whereas the emissivity of vegetation, water, and ice cover are generally greater than 0.95 and spectrally flat in the 8–12- $\mu\text{m}$  range.

### 2.2.1.3 Radiative Transfer Model

The current choice of radiative transfer model for atmospherically correcting VIIRS TIR data is the Radiative Transfer for TOVS (RTTOV). The RTTOV is a very fast radiative transfer model for nadir-viewing passive visible, infrared and microwave satellite radiometers, spectrometers and interferometers (Saunders et al. 1999). RTTOV is a FORTRAN-90 code for simulating satellite radiances, designed to be incorporated within users' applications. RTTOV was originally developed at ECMWF in the early 90's for TOVS (Eyre and Woolf 1988). Subsequently the original code has gone through several developments (Matricardi et al. 2001; Saunders et al. 1999), more recently within the EUMETSAT NWP Satellite Application Facility (SAF), of which RTTOV v11 is the latest version. It is actively developed by ECMWF and UKMET.

A number of satellite sensors are supported from various platforms (<https://nwp-saf.eumetsat.int/site/software/rttov/documentation/platforms-supported/>). RTTOV has been sufficiently tested and validated and is conveniently fast for full scale retrievals (Matricardi 2009). Given an atmospheric profile of temperature, water vapor and optionally other trace gases (for example ozone and carbon dioxide) together with satellite and solar zenith angles and surface temperature, pressure and optionally surface emissivity and reflectance, RTTOV will compute the top of atmosphere radiances in each of the channels of the sensor being simulated. Users can also specify the selected channels to be simulated.

Mathematically, in vector notation, given a state vector,  $\mathbf{x}$ , which describes the atmospheric/surface state as a profile and surface variables the radiance vector,  $\mathbf{y}$ , for all the channels required to be simulated is given by (Saunders et al. 1999):

$$\mathbf{y} = H(\mathbf{x}) \tag{5}$$

where  $H$  is the radiative transfer model, i.e. RTTOV (also referred to as the observation operator in data assimilation parlance). This is known as the 'direct' or 'forward' model.

In RTTOV, the transmittances of the atmospheric gases are expressed as a function of profile dependent predictors. This parameterization of the transmittances makes the model computationally efficient. The RTTOV fast transmittance scheme uses regression coefficients derived from accurate Line by Line computations to express the optical depths as a linear combination of profile dependent predictors that are functions of temperature, absorber amount, pressure and viewing angle (Matricardi and Saunders 1999). The regression coefficients are computed using a training set of diverse atmospheric profiles chosen to represent the range of variations in temperature and absorber amount found in the atmosphere (Chevallier 2000; Matricardi 2008, 2009; Matricardi and Saunders 1999). The selection of the predictors is made according to the coefficients file supplied to the program.

#### *2.2.1.4 Atmospheric Profiles*

The general methodology for atmospherically correcting VIIRS TIR data is based on the methods that were developed for the ASTER (Palluconi et al. 1999) and MODIS approaches (Hulley et al. 2012).

Currently two options for atmospheric profile sources are available: 1) interpolation of data assimilated from NWP models, and 2) retrieved atmospheric geophysical profiles from remote-sensing data. The NWP models use current weather conditions, observed from various sources (e.g., radiosondes, surface observations, and weather satellites) as input to dynamic mathematical models of the atmosphere to predict the weather. Data are typically output in 6-hour increments, e.g., 00, 06, 12, and 18 UTC. Examples include the Global Data Assimilation System (GDAS) product provided by the National Centers for Environmental Prediction (NCEP) (Kalnay et al. 1990), the Modern Era Retrospective-analysis for Research and Applications (MERRA) product provided by the Goddard Earth Observing System Data Assimilation System Version 5.2.0 (GEOS-5.2.0) (Bosilovich et al. 2008), and the European Center for Medium-Range Weather Forecasting (ECMWF), which is supported by more than 32 European states. Remote-sensing data, on the other hand, are available real-time, typically twice-daily and for clear-sky conditions. The principles of inverse theory are used to estimate a geophysical state (e.g., atmospheric temperature) by measuring the spectral emission and absorption of some known chemical species such as carbon dioxide in the thermal infrared region of the electromagnetic spectrum (i.e. the observation). Examples of current remote sensing data include the Atmospheric Infrared Sounder (AIRS)

(Susskind et al. 2003) and Moderate Resolution Imaging Spectroradiometer (MODIS) (Justice and Townshend 2002), both on NASA's Aqua satellite launched in 2002.

The VIIRS TES algorithm uses the MERRA-2 reanalysis data for atmospheric correction. The MERRA profiles are first interpolated in time to the VIIRS observation using the [00 06 12 18] UTC analysis observation hours before ingesting into the RTTOV.

**Table 1: Geophysical data available in the MERRA-2 reanalysis product. Columns under Mandatory specify if the variables is needed for determining atmospheric correction parameters. Data are output in 6hr analysis for 42 pressure levels at 1/2 degree x 2/3 degree spatial resolution (longitude=576, latitude=361).**

MERRA Analysis Data (inst6_3d_ana_Np)				
Geophysical fields		Required?	Available?	Remarks
time	Time	Yes	Yes	
lat	Latitude	Yes	Yes	
lon	Longitude	Yes	Yes	
nlev	nLevel	Yes	Yes	
p	Pressure	Yes	Yes	
t	Temperature	Yes	Yes	
q	Specific Humidity	Yes	Yes	
sp	Surface Pressure	Yes	Yes	
skt	Skin Temperature	Yes	No	T value at the first valid level above surface is used.
t2	Temperature at 2 m	Yes	No	T value at the first valid level above surface is used
q2	Specific Humidity at 2 m	Yes	No	Q value at the first valid level above surface is used
ism	Land Sea Mask	Yes	No	Auxiliary database
el	Elevation	Yes	No	Auxiliary database

The RTTOV output data are then gridded to the VIIRS swath resolution using a bicubic interpolation approach. It should be noted that the data interpolation could potentially introduce errors, especially in humid regions where atmospheric water vapor can vary on smaller spatial scales than 1°. The propagation of these atmospheric correction errors would result in band-dependent surface radiance errors in both spectral shape and magnitude, which in turn could result in errors of retrieved Level-2 products such as surface emissivity and temperature. As a result, a Water Vapor Scaling (WVS) model is further employed to improve the accuracy of the

atmospheric correction during atmospheric conditions with high water vapor loadings. The WVS approach is discussed in the following section.

### 2.2.2 Water Vapor Scaling Method

The accuracy of the TES algorithm is limited by uncertainties in the atmospheric correction, which result in a larger apparent emissivity contrast. This intrinsic weakness of the TES algorithm has been systemically analyzed by several authors (Coll et al. 2007; Gillespie et al. 1998; Gustafson et al. 2006; Hulley and Hook 2009b; Li et al. 1999), and its effect is greatest over graybody surfaces that have a true spectral contrast that approaches zero. In order to minimize atmospheric correction errors, a Water Vapor Scaling (WVS) method has been introduced to improve the accuracy of the water vapor atmospheric profiles on a band-by-band basis for each observation using an Extended Multi-Channel/Water Vapor Dependent (EMC/WVD) algorithm (Tonooka 2005), which is an extension of the Water Vapor Dependent (WVD) algorithm (Francois and Otle 1996). The EMC/WVD equation models the at-surface brightness temperature, given the at-sensor brightness temperature, along with an estimate of the total water vapor amount:

$$T_{g,i} = \alpha_{i,0} + \sum_{k=1}^n \alpha_{i,k} T_k \quad (6)$$

$$\alpha_{i,k} = p_{i,k} + q_{i,k}W + r_{i,k}W^2,$$

where:

$i$	Band number
$n$	Number of bands
$W$	Estimate of total precipitable water vapor (cm)
$p, q, r$	Regression coefficients for each band
$T_k$	Brightness temperature for band k (K)
$T_{g,i}$	Brightness surface temperature for band, $i$

The coefficients of the EMC/WVD equation are determined using a global-based simulation model.

The scaling factor,  $\gamma$ , used for improving a water profile, is based on the assumption that the transmissivity,  $\tau_i$ , can be expressed by the Pierluissi double exponential band model formulation. The scaling factor is computed for each gray pixel on a scene using  $T_{g,i}$  computed from equation (4) and  $\tau_i$  computed using two different  $\gamma$  values that are selected *a priori*:

$$\gamma^{\alpha_i} = \frac{\ln \left( \frac{\tau_i(\theta, \gamma_2)^{\gamma_1^{\alpha_i}}}{\tau_i(\theta, \gamma_1)^{\gamma_2^{\alpha_i}}} \cdot \left( \frac{B_i(T_{g,i}) - L_i^\uparrow(\theta, \gamma_1)/(1 - \tau_i(\theta, \gamma_1))}{L_i - L_i^\uparrow(\theta, \gamma_1)/(1 - \tau_i(\theta, \gamma_1))} \right)^{\gamma_1^{\alpha_i} - \gamma_2^{\alpha_i}} \right)}{\ln(\tau_i(\theta, \gamma_2)/\tau_i(\theta, \gamma_1))} \quad (7)$$

where:

- $\alpha_i$  Band model parameter
- $\gamma_1, \gamma_2$  Two appropriately chosen  $\gamma$  values
- $\tau_i(\theta, \gamma_{1,2})$  Transmittance calculated with water vapor profile scaled by  $\gamma$
- $L_i^\uparrow(\theta, \gamma_{1,2})$  Path radiance calculated with water vapor profile scaled by  $\gamma$

Typical values for  $\gamma$  are  $\gamma_1 = 1$  and  $\gamma_2 = 0.7$ . Tonooka (2005) found that the  $\gamma$  calculated by equation (7) will not only reduce biases in the water vapor profile, but will also simultaneously reduce errors in the air temperature profiles and/or elevation. Figure 4 shows an example of a  $\gamma$  image.

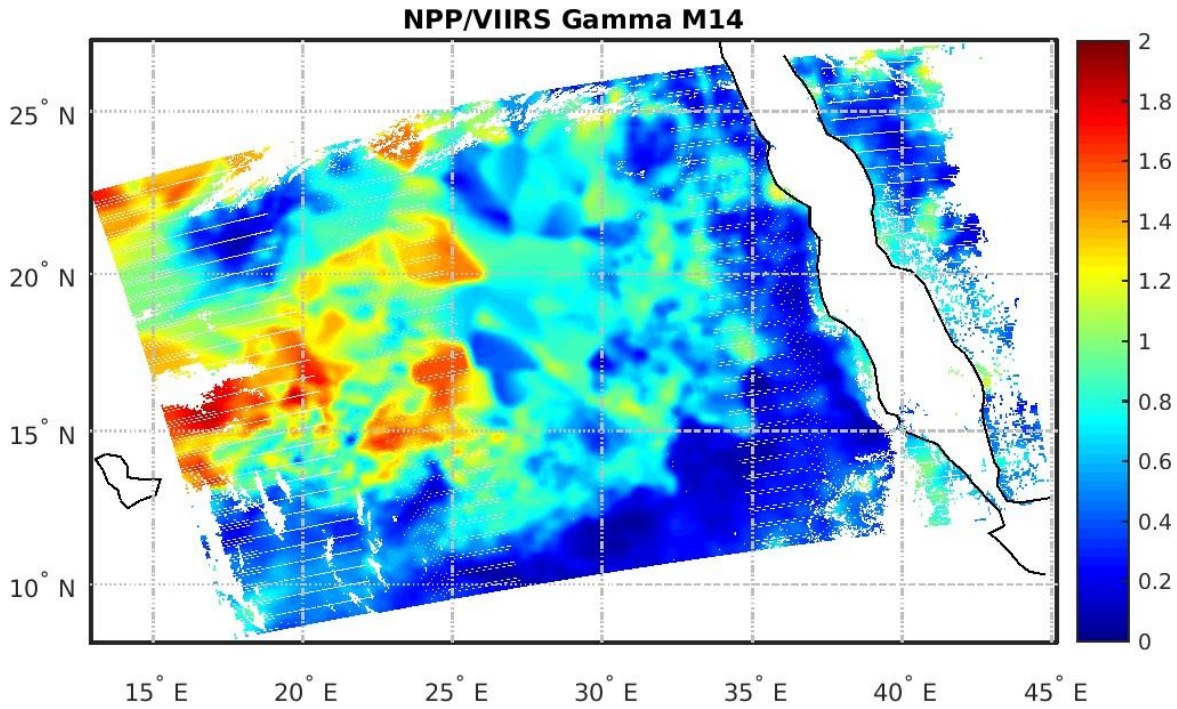


Figure 4. WVS factor  $\gamma$  computed for a VIIRS scene on 13 January 2014. The image has been interpolated and smoothed.

### 2.2.2.1 Scaling Atmospheric Parameters

Once the RTTOV run has completed and the  $\gamma$  image has been calculated, the atmospheric parameters transmittance  $\tau_i$  and path radiance  $L_i^\uparrow$  are modified as follows:

$$\tau_i(\theta, \gamma) = \tau_i(\theta, \gamma_1)^{\frac{\gamma_1^{\alpha_i} - \gamma_2^{\alpha_i}}{\gamma_1^{\alpha_i} - \gamma_2^{\alpha_i}}} \cdot \tau_i(\theta, \gamma_2)^{\frac{\gamma_1^{\alpha_i} - \gamma_2^{\alpha_i}}{\gamma_1^{\alpha_i} - \gamma_2^{\alpha_i}}} \quad (8)$$

$$L_i^\uparrow(\theta, \gamma) = L_i^\uparrow(\theta, \gamma_1) \cdot \frac{1 - \tau_i(\theta, \gamma)}{1 - \tau_i(\theta, \gamma_1)} \quad (9)$$

Once the transmittance and path radiance have been adjusted using the scaling factor, the surface radiance can be computed using equation (1).

### 2.2.2.2 Calculating the EMC/WVD Coefficients

The EMC/WVD coefficients,  $(p, q, r)$  in Eq. (6) are determined using a global simulation model with input atmospheric parameters from SeeBor V5.0 database provided by the University of Wisconsin-Madison (Hook et al. 2013). The SeeBor data consists of 15704 global profiles of uniformly distributed global atmospheric soundings temperature, moisture, and ozone at 101 pressure levels for clear sky conditions, acquired both day and night in order to capture the full-scale natural atmospheric variability. These profiles are taken from NOAA-88, an ECMWF 60L training set, TIGR-3, ozonesondes from 8 NOAA Climate Monitoring and Diagnostics Laboratory (CMDL) sites, and radiosondes from 2004 in the Sahara desert. The Seebor data are curated with the following quality criteria: for clear sky conditions, the relative humidity (RH) value of the profiles must be less than 99 % at each level below the 250 hPa pressure level. It also is required that the original top of sounding pressure be no greater than 30 hPa for temperature and moisture profiles and 10 hPa for ozone, and for each profile in the data set a physically based characterization of the surface skin temperature and surface emissivity are assigned. As the radiosondes may drift towards water body, we further filter the data containing at least 50% of the records on the land. This resulted into the sample size to 9136 data points. When classified based upon the local sun-rise and sun-set times the day and night profiles are nearly equally distributed in counts at 4990 and 4142 respectively. Figure 5 shows the distribution of the surface temperature with the total precipitable water (tpw) in cm for the profiles used in the simulation.

Figure 6 shows the global distribution of the profile locations, which have been indicated as the day/night profiles based upon the sun-rise/sun-set time at the time of the profile recordings.



In order to perform the simulations, we consider the emissivity spectra from the ASTER spectral library consisting of 102 samples that includes a variety of materials such as water, snow/ice, vegetation, rocks, soils, and sands. The emissivity of the samples cover a broad range of emissivities with even distribution ranging from ~0.6 to 1. The selected spectra are then convolved to the VIIRS's spectral response function (3 bands: M14, M15, and M16) in order to perform the simulation. A total of 931,872 simulations (9136 profiles x 102 samples) are simulated with the RTTOV radiative transfer model for the set of 11 Gaussian view angles (between 0-70°), and for the three VIIRS TIR bands. Using the simulated at-sensor  $T_k$ , and at-surface  $T_g$  calculated brightness temperatures, and an estimate of the total precipitable water vapor, the best fit coefficients in Eq. (3) are found by using a linear least squares method, and dependent on four independent variables: day/night case, view angle, minimum band emissivity in intervals of 0.05, and precipitable water vapor. Simulations show that for all of these cases the RMSE error for the simulation was less than 1 K. Finally, a four-dimensional look-up table (LUT) is produced consisting of the regression coefficients for the three TIR bands and the four independent variables. The EMC/WVD LUT is then used on a pixel-by-pixel basis for calculating the  $T_g$  (and  $\gamma$ ), given estimates of the view angle, emissivity, and PWV. Note that the EMC/WVD coefficients are mapped to all VIIRS pixels in a granule through bi-cubic interpolation of the coefficients derived from the four factors: day/night case, view angle, minimum band emissivity, and precipitable water vapor. ASTER GED v3 emissivities are first spectrally adjusted to VIIRS TIR bands and interpolated onto the VIIRS granule, and then the minimum band emissivity is calculated at each VIIRS pixel in order to assign the correct coefficients. Bi-cubic interpolation assures smooth transitions in the EMC/WVD coefficients across the pixels. Table 2 shows the band model parameter coefficients used in equation (7) to calculate the water vapor scaling factor.

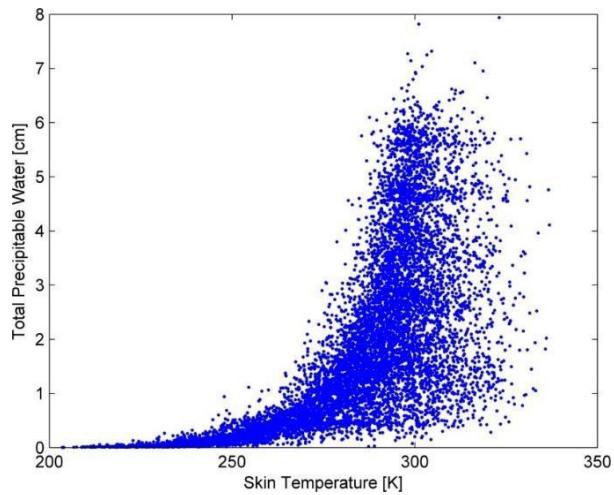


Figure 5. TPW Vs Skin Temperature plot showing the wide distribution of input profiles.

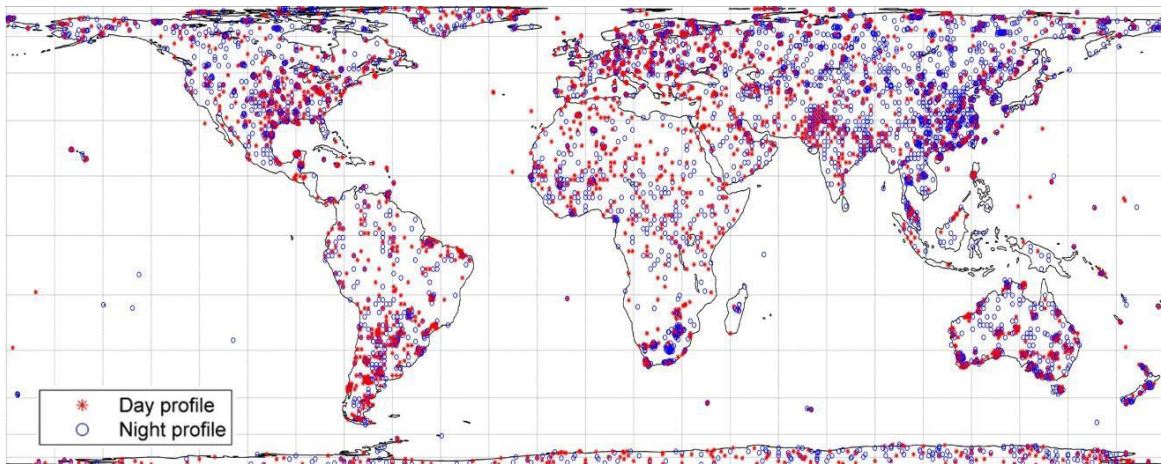


Figure 6. Global SeeBor database showing station locations for day and night sondes.

Table 2. VIIRS band model parameters in equation (6).

Band	Parameter
M14	1.4522
M15	1.8103
M16	1.8056

### 2.2.3 TES Algorithm

TES combines the NEM, the ratio, and the MMD algorithm to retrieve temperature and a full emissivity spectrum. The NEM algorithm is used to estimate temperature and iteratively remove the sky irradiance, from which an emissivity spectrum is calculated, and then ratioed to their mean value in the ratio algorithm. At this point, only the shape of the emissivity spectrum is preserved, but not the amplitude. In order to compute an accurate temperature, the correct amplitude is then found by relating the minimum emissivity to the spectral contrast (MMD). Once the correct emissivities are found, a final temperature can be calculated with the maximum emissivity value. Additional improvements involve a refinement of  $\epsilon_{max}$  in the NEM module and refining the correction for sky irradiance using the  $\epsilon_{min}$ -MMD final emissivity and temperature values. Finally, a quality assurance (QA) data image is produced that partly depends on outputs from TES such as convergence, final  $\epsilon_{max}$ , atmospheric humidity, and proximity to clouds. More detailed discussion of QA is included later in this document.

Numerical modeling studies performed by the ASTER TEWG showed that TES can recover temperatures to within 1.5 K and emissivities to within 0.015 over most scenes, assuming well-calibrated, accurate radiometric measurements (Gillespie et al. 1998).

#### 2.2.3.1 TES Data Inputs

Inputs to the TES algorithm are the surface radiance,  $L_{s,i}$ , given by equation (4) (at-sensor radiance corrected for transmittance and path radiance), and downwelling sky irradiance term,  $L_{\lambda}^{\downarrow}$ , which is computed from the atmospheric correction algorithm using a radiative transfer model such as RTTOV. Both the surface radiance and sky irradiance will be output as a separate product. The surface radiance is primarily used as a diagnostic tool for monitoring changes in Earth's surface composition. Before the surface radiance is estimated using equation (4), the accuracy of the atmospheric parameters,  $L_{\lambda}^{\downarrow}$ ,  $\tau_{\lambda}(\theta)$ ,  $L_{\lambda}^{\uparrow}(\theta)$ , is improved upon using a WVS method (Tonooka 2005) on a band-by-band basis for each observation using an extended multi-channel/water vapor dependent (EMC/WVD) algorithm.

#### 2.2.3.2 TES Limitations

As with any retrieval algorithm, limitations exist that depend on measurement accuracy, model errors, and incomplete characterization of atmospheric effects. Currently, the largest source of uncertainty for ASTER data is the residual effect of incomplete atmospheric correction.

Measurement accuracy and precision contribute to a lesser degree. This problem is compounded for graybodies, which have low spectral contrast and are therefore more prone to errors in “apparent” MMD, which is overestimated due to residual sensor noise and incomplete atmospheric correction. A threshold classifier was introduced by the TEWG to partly solve this problem over graybody surfaces. Instead of using the calibration curve to estimate  $\epsilon_{min}$  from MMD, a value of  $\epsilon_{min}= 0.983$  was automatically assigned when the spectral contrast or MMD in emissivity was smaller than 0.03 for graybody surfaces (e.g., water, vegetation). However, this caused artificial step discontinuities in emissivity between vegetated and arid areas.

At the request of users, two parameter changes were made to the ASTER TES algorithm on 1 August 2007, first described in Gustafson et al. (2006). Firstly, the threshold classifier was removed as it caused contours and artificial boundaries in the images, which users could not tolerate in their analyses. The consequence of removing the threshold classifier was a smoother appearance for all images but at the cost of TES underestimating the emissivity of graybody scenes, such as water by up to 3% and vegetation by up to 2% (Hulley et al. 2008). The second parameter change removed the iterative correction for reflected downwelling radiation, which also frequently failed due to inaccurate atmospheric corrections (Gustafson et al. 2006). Using only the first iteration resulted in improved spectral shape and performance of TES.

### 2.2.3.3 TES Processing Flow

Figure 7 shows the processing flow diagram for the generation of the cloud masks, land-leaving radiance, VNIR reflectances, and TES temperature and emissivity, while Figure 8 shows a more detailed processing flow of the TES algorithm itself. Each of the steps will be presented in sufficient detail in the following section, allowing users to regenerate the code. TES uses input image data of surface radiance,  $L_{s,i}$ , and sky irradiance,  $L_{\lambda}^{\downarrow}$ , to solve the TIR radiative transfer equation. The output images will consist of three emissivity images ( $\epsilon_i$ ) corresponding to VIIRS bands M14, M15, M16, and one surface temperature image (T).

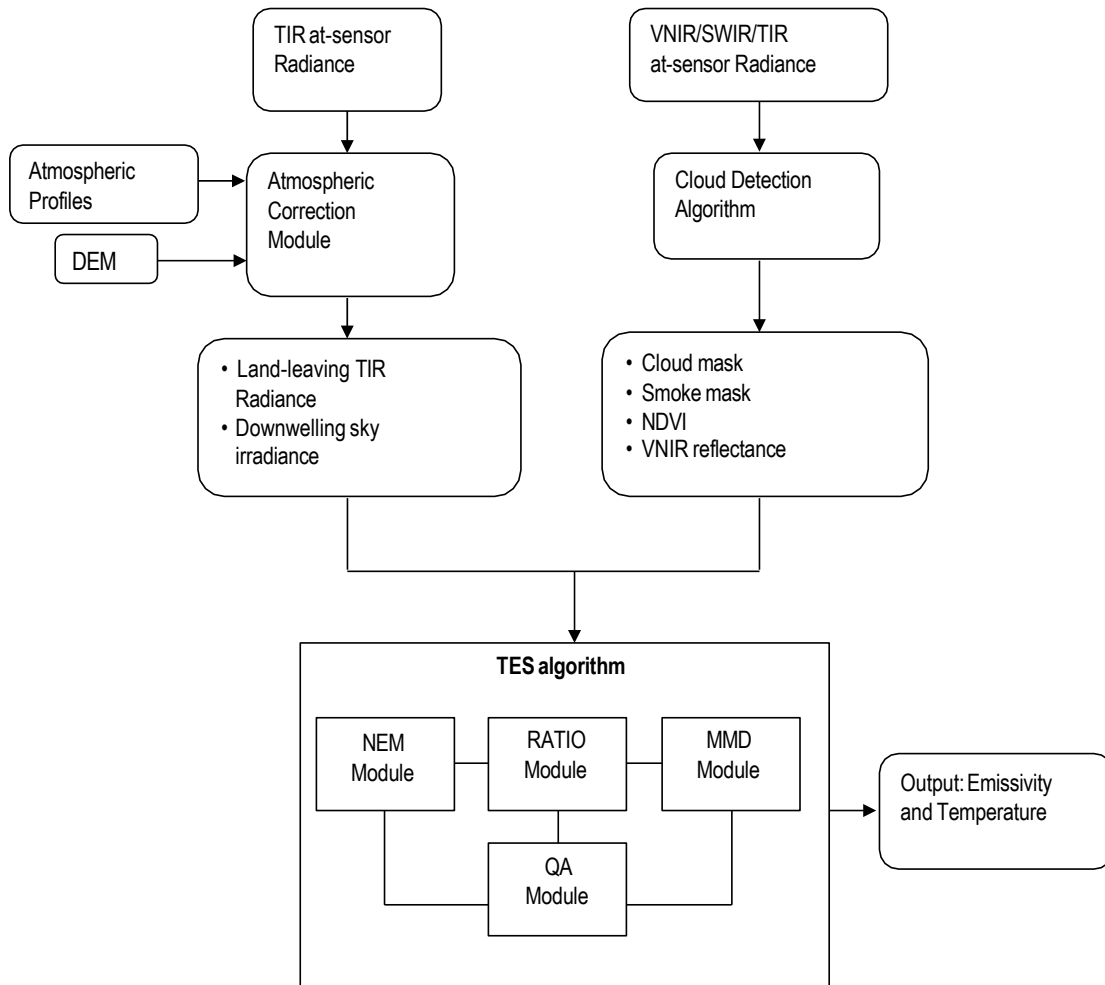


**Figure 7. Flow diagram showing all steps in the retrieval process in generating the VIIRS VNP21 LST&E product starting with TIR at-sensor radiances and progressing through atmospheric correction, cloud detection, and the TES algorithm.**

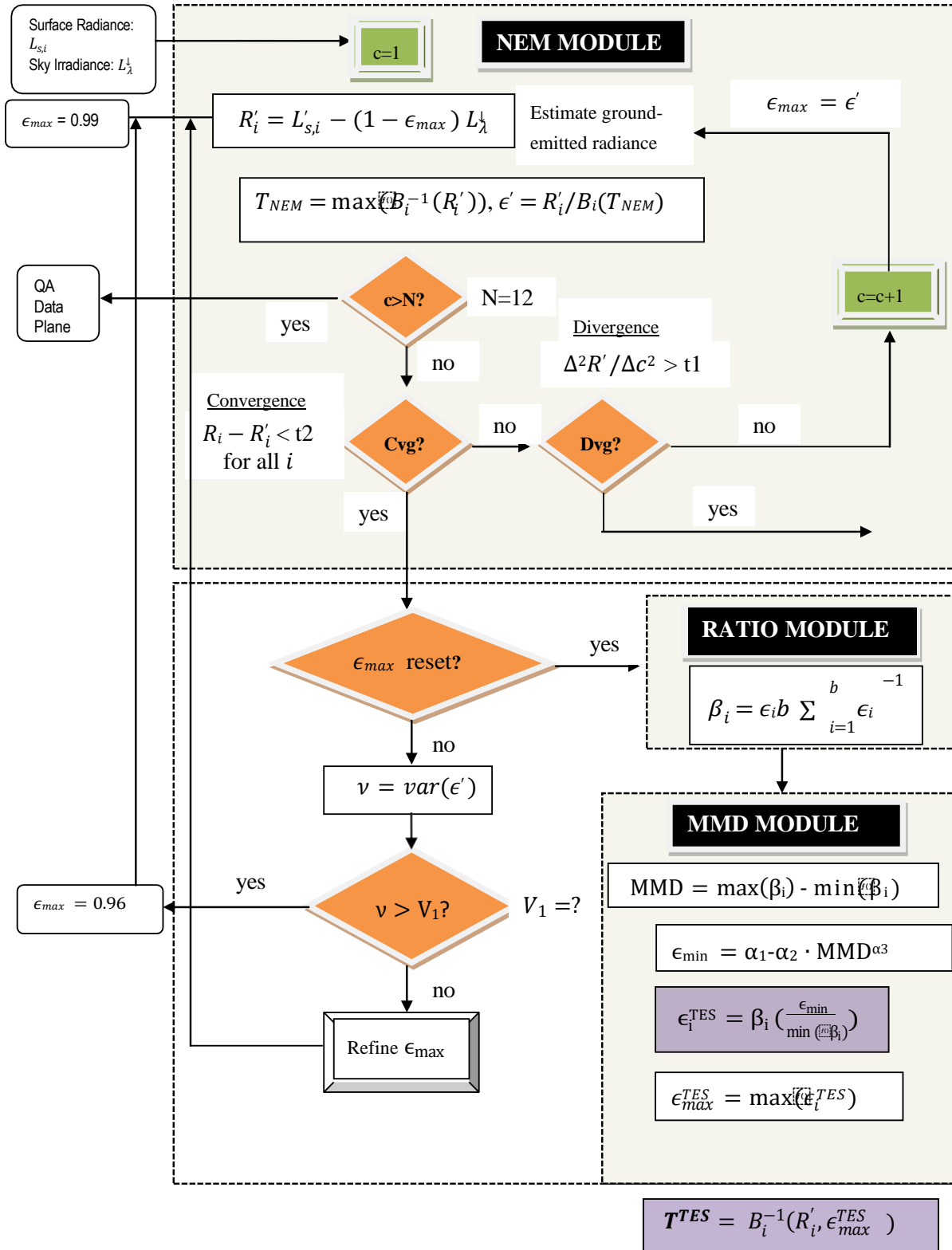


Figure 8. Flow diagram of the TES algorithm in its entirety, including the NEM, RATIO, and MMD modules. Details are included in the text, including information about the refinement of  $\epsilon_{max}$ .

#### 2.2.3.4 NEM Module

The NEM builds upon the model emissivity algorithm (Lyon 1965) by allowing the initial  $\epsilon_{max}$  value to be consistent for all wavelengths. The role of NEM is to compute the surface kinetic temperature,  $T$ , and a correct shape for the emissivity spectrum. An initial value of 0.99 is set for  $\epsilon_{max}$ , which is typical for most vegetated surfaces, snow, and water. For geologic materials such as rocks and sand,  $\epsilon_{max}$  values are set lower than this, typically 0.96, and this value remains fixed. For all other surface types, a modification to the original NEM allows for optimization of  $\epsilon_{max}$  using an empirically based process. For the majority of materials in the ASTER spectral library, a typical range for  $\epsilon_{max}$  is  $0.94 < \epsilon_{max} < 1.0$ . Therefore, for a material at 300 K, the maximum errors that NEM temperatures should have are  $\sim \pm 1.5$  K, assuming the reflected sky irradiance has been estimated correctly.

#### 2.2.3.5 Subtracting Downwelling Sky Irradiance

Generally the effects of sky irradiance are small with typical corrections of  $< 1$  K (Gillespie et al. 1998). However, the contribution becomes larger for pixels with low emissivity (high reflectance) or in humid conditions when the sky is warmer than the surface. Over graybody surfaces (water and vegetation), the effects are small because of their low reflectivity in all bands. The first step of the NEM module is to estimate ground-emitted radiance, which is found by subtracting the reflected sky irradiance from the surface radiance term:

$$R_i = L'_{s,i} - (1 - \epsilon_{max}) L_{\lambda}^{\downarrow} \quad (10)$$

The NEM temperature, which we call  $T_{NEM}$ , is then estimated by inverting the Planck function for each band using  $\epsilon_{max}$  and the ground-emitted radiance and then taking the maximum of those temperatures. The maximum temperature will most likely be closest to the actual surface temperature in the presence of uncompensated atmospheric effects.

$$T_i = \frac{c_2}{\lambda_i} \left( \ln \left( \frac{c_1 \epsilon_{max}}{\pi R_i \lambda_i^5} + 1 \right) \right)^{-1} \quad (11)$$

$$T_{NEM} = \max(T_i) \quad (12)$$

The NEM emissivity spectrum is then calculated as the ratio of emitted radiance to that of a blackbody with a temperature estimated by  $T_{NEM}$ :

$$\epsilon'_i = \frac{R_i}{B_i(T_{NEM})} \quad (13)$$

The new emissivity spectrum is then used to re-calculate  $R'_i = L'_{s,i} - (1 - \epsilon'_i) L^\downarrow_\lambda$ , and the process is repeated until convergence, which is determined if the change in  $R_i$  between steps is less than a set threshold,  $t_2$ , which is set as the radiance equivalent to NE $\Delta$ T of the sensor. The process is stopped if the number of iterations exceeds a limit  $N$ , set to 12. Execution of the NEM module is also aborted if the slope of  $R_i$  versus iteration,  $c$ , increases such that  $\Delta^2 R' / \Delta c^2 > t_1$ , where  $t_1$  is also set to radiance equivalent of NE $\Delta$ T for the sensor ( $\sim 0.05$  K for VIIRS). In this case, correction is not possible, TES is aborted, and NEM values of  $\epsilon_i$  and  $T_{NEM}$  are reported in the QA data plane, along with an error flag. TES is also aborted and an error flag recorded if, for any iteration, the values of  $\epsilon_i$  fall out of reasonable limits, set to  $0.5 < \epsilon_i < 1.0$ . See Figure 8 for a detailed description of these steps.

#### 2.2.3.6 Refinement of $\epsilon_{max}$

Most pixels at VIIRS resolution (750 m) will contain a mixed cover type consisting of vegetation and soil, rock and water. The effective maximum emissivity for such pixels will therefore vary across the scene and depend on the fractional contribution of each cover type. For these cases, the initial  $\epsilon_{max} = 0.99$  may be set to high and refinement of  $\epsilon_{max}$  is necessary to improve accuracy of  $T_{NEM}$ . The optimal value for  $\epsilon_{max}$  minimizes the variance,  $\nu$ , of the NEM calculated emissivities,  $\epsilon_i$ . The optimization of  $\epsilon_{max}$  is only useful for pixels with low emissivity contrast (near graybody surfaces) and therefore is only executed if the variance for  $\epsilon_{max} = 0.99$  is less than an empirically determined threshold (e.g.,  $V_1 = 1.7 \times 10^{-4}$  for ASTER) (Gillespie et al. 1998). If the variance is greater than  $V_1$ , then the pixel is assumed to predominately consist of either rock or soil. For this case,  $\epsilon_{max}$  is reset to 0.96, which is a good first guess for most rocks and soils in the ASTER spectral library, which typically fall between the 0.94 and 0.99 range. For VIIRS the  $\epsilon_{max}$  values is set to 0.97, a typical value for bare surfaces in the 12  $\mu$ m range. If the first condition is met, and the pixel is a near-graybody, then values for  $\epsilon_{max}$  of 0.92, 0.95, 0.97, and 0.99 are used to compute the variance for each corresponding NEM emissivity spectrum. A plot of variance  $\nu$  versus each  $\epsilon_{max}$  value results in an upward-facing parabola with the optimal  $\epsilon_{max}$  value determined by the minimum of the parabola curve in the range  $0.9 < \epsilon_{max} < 1.0$ . This minimum is set to a new  $\epsilon_{max}$  value, and the NEM module is executed again to compute a new  $T_{NEM}$ . Further tests are used to see if a reliable solution can be found for the refined  $\epsilon_{max}$ . If the parabola is too flat, or too steep, then refinement is aborted and the original  $\epsilon_{max}$  value is used.



The steepness condition is met if the first derivative (slope of  $\nu$  vs.  $\epsilon_{max}$ ) is greater than a set threshold (e.g.,  $V_2 = 1.0 \times 10^{-3}$  for ASTER) and the flatness conditions is met if the second derivative is less than a set threshold (e.g.,  $V_3 = 1.0 \times 10^{-3}$  for ASTER). Finally, if the minimum  $\epsilon_{max}$  corresponds to a very low  $\nu$ , then the spectrum is essentially flat (graybody) and the original  $\epsilon_{max} = 0.99$  is used. This condition is met if  $\nu_{min} < V_4$  (e.g.,  $V_2 = 1.0 \times 10^{-4}$ ).

### 2.2.3.7 Ratio Module

In the ratio module, the NEM emissivities are ratioed to their average value to calculate a  $\beta_i$  spectrum as follows:

$$\beta_i = \frac{\epsilon_i}{\bar{\epsilon}} \quad (14)$$

Typical ranges for the  $\beta_i$  emissivities are  $0.75 < \beta_i < 1.32$ , given that typical emissivities range from 0.7 to 1.0. Errors in the  $\beta_i$  spectrum due to incorrect NEM temperatures are systematic.

### 2.2.3.8 MMD Module

In the MMD module, the  $\beta_i$  emissivities are scaled to an actual emissivity spectrum using information from the spectral contrast or MMD of the  $\beta_i$  spectrum. The MMD can then be related to the minimum emissivity,  $\epsilon_{min}$ , in the spectrum using an empirical relationship determined from lab measurements of a variety of different spectra, including rocks, soils, vegetation, water, and snow/ice. From  $\epsilon_{min}$ , the actual emissivity spectrum can be found by re-scaling the  $\beta_i$  spectrum. First, the MMD of the  $\beta_i$  spectrum is found by:

$$MMD = \max(\beta_i) - \min(\beta_i) \quad (15)$$

Then MMD can be related to  $\epsilon_{min}$  using a power-law relationship:

$$\epsilon_{min} = \alpha_1 - \alpha_2 MMD^{\alpha_3}, \quad (16)$$

where  $\alpha_j$  are coefficients that are obtained by regression using lab measurements.

The relationship between MMD and  $\epsilon_{min}$  is physically reasonable and is determined using a set of laboratory spectra in the ASTER spectral library v2.0 (Baldrige et al. 2009) and referred to as the calibration curve. The original ASTER regression coefficients were determined from a set of 86 laboratory reflectance spectra of rocks, soils, water, vegetation, and snow supplied by J.W. Salisbury from Johns Hopkins University. One question that needed to be answered was whether using a smaller or larger subset of this original set of spectra changed the results in any manner. Establishing a reliable MMD vs.  $\epsilon_{min}$  relationship with a subset of spectral representing all types of surfaces is a critical assumption for the calibration curve. This assumption

was tested using various combinations and numbers of different spectra (e.g., Australian rocks, airborne data, and a subset of 31 spectra from Salisbury), and all yielded very similar results to the original 86 spectra.

For VIIRS, the original 86 spectra were updated to include additional sand spectra used to validate the North American ASTER Land Surface Emissivity Database (NAALSED) (Hulley and Hook 2009b) and additional spectra for vegetation from the MODIS spectral library and ASTER spectral library v2.0, giving a total of 150 spectra. The data were convolved to the three VIIRS TIR bands and  $\epsilon_{min}$  and  $\beta_i$  spectra calculated using equation (20) for each sample. The MMD for each spectrum was then calculated from the  $\beta_i$  spectra and regressed to the  $\epsilon_{min}$  values. The relationship follows a simple power law given by equation (22), with regression coefficients  $\alpha_1=0.997$ ,  $\alpha_2 = 0.7050$ , and  $\alpha_3 = 0.7430$  (graybody), and as  $\alpha_1=0.9864$ ,  $\alpha_2 = 0.7711$ , and  $\alpha_3 = 0.8335$  (desert). Figure 9 shows the power-law relationship between MMD and  $\epsilon_{min}$  using the 150 lab spectra.

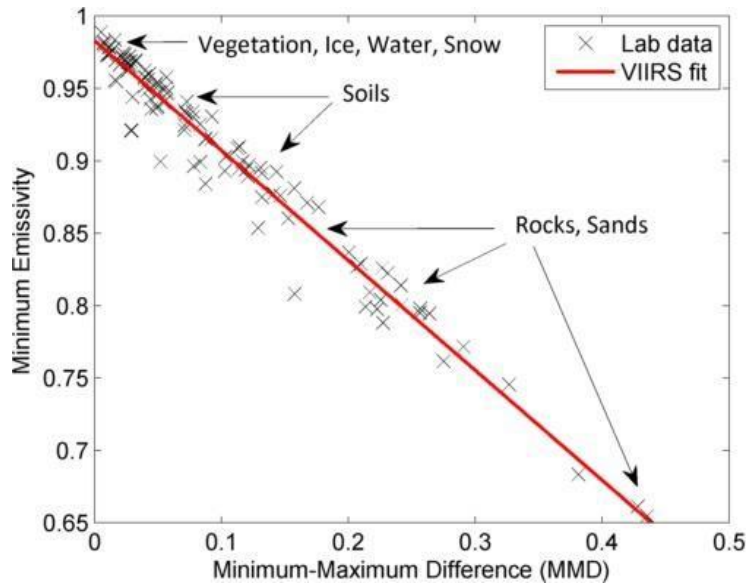
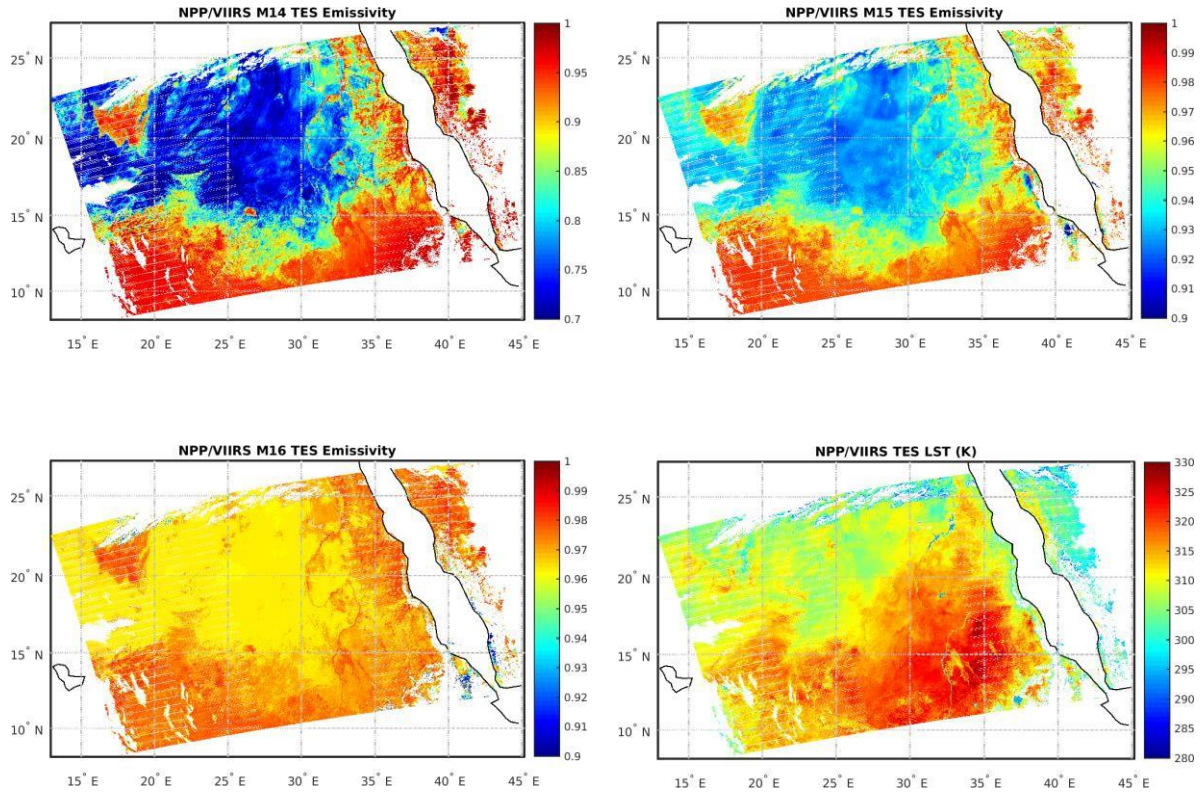


Figure 9. VIIRS calibration curve of minimum emissivity vs. MMD. The lab data (crosses) are computed from 150 spectra consisting of a broad range of terrestrial materials (rocks, sand, soil, water, vegetation, and ice).

The TES emissivities are then calculated by re-scaling the  $\beta_i$  emissivities:

$$\epsilon_i^{TES} = \beta_i \left( \frac{\epsilon_{min}}{\min(\beta_i)} \right) \quad (17)$$



**Figure 10. Clockwise from top left: VIIRS land surface emissivity for band M14 (8.55  $\mu\text{m}$ ); band M15 (10.76  $\mu\text{m}$ ), surface temperature (K) and band M15 emissivity (12  $\mu\text{m}$ ); output from the TES algorithm over northeast Africa on 13 January 2014.**

An example VNP21 emissivity output image for band M14 (8.55  $\mu\text{m}$ ) is shown in Figure 10 for one VIIRS granule on 13 January 2015 over the Sahara desert. Bare areas generally have emissivity  $<0.85$ , while graybody surfaces have higher emissivities,  $>0.95$ . Corresponding VNP21 surface temperature output image is shown in Figure 10.

Note that, for pixels with low spectral contrast (e.g., graybody surfaces), the accuracy of MMD calculated from TES is compromised and approaches a value that depends on measurement error and residual errors from incomplete atmospheric correction. For ASTER, which has a NEAT of 0.3 K at 300 K, measurement error contributes to the apparent contrast, and a method was explored to correct the apparent MMD using Monte Carlo simulations. For VIIRS (NEAT of 0.05 K), we expect measurement errors to be minimal and atmospheric effects to be the largest contribution to MMD errors. A further problem for graybody surfaces is a loss of precision for low MMD values. This is due to the shape of the power-law curve of  $\epsilon_{min}$  vs. MMD at low MMD

values, where small changes in MMD can lead to large changes in  $\epsilon_{min}$ . To address these issues, the ASTER TEWG initially proposed a threshold classifier for graybody surfaces.

If  $MMD < 0.03$ , the value of  $\epsilon_{min}$  in equation (22) was set to 0.983, a value typical for water and most vegetated surfaces. However, this classification was later abandoned as it introduced large step discontinuities in most images (e.g., from vegetation to mixed-cover types). The consequence of removing the threshold classifier was that, over graybody surfaces, errors in emissivity could range from 0.01 to 0.05 (0.5 K to 3 K) due to measurement error and residuals errors from atmospheric correction (Gustafson et al. 2006; Hulley and Hook 2009b). For VNP21, we use original TES without classification and the WVS method to correct the atmospheric parameters on a pixel-by-pixel basis.

For bare surfaces (rocks, soils, and sand), the error in NEM-calculated T may be as much as 2–3 K, assuming a surface at 340 K due to the fixed assumption of  $\epsilon_{max} = 0.96$ . This error can be corrected by recalculating T using the TES retrieved maximum emissivity,  $\epsilon_{max}^{TES}$ , and the atmospherically corrected radiances,  $R_i$ . The maximum emissivity used as correction for reflected  $L_{\lambda}^{\downarrow}$  will be minimal.

$$T^{TES} = \frac{c_2}{\lambda_{max}} \left( \ln \left( \frac{c_1 \epsilon_{max}^{TES}}{\pi R_i \lambda_{max}^5} + 1 \right) \right)^{-1} \quad (18)$$

In the original ASTER TES algorithm, a final correction is made for sky irradiance using the TES temperature and emissivities; however, this was later removed, as correction was minimal and influenced by atmospheric correction errors. This additional correction is not used for the VNP21 algorithm.

### 2.2.3.9 Atmospheric Effects

The accuracy of the atmospheric correction technique used to estimate the surface radiance relies on the accuracy of the variables input to the radiative transfer model (e.g., air temperature, relative humidity, and ozone). These atmospheric errors tend to be highly correlated from band to band, since each channel has a characteristic absorbing feature. As a result, the effect on TES output is usually relatively small, but if these errors are uncorrelated from band to band then much larger errors can occur, particularly for graybodies, where small changes in MMD can significantly alter the shape of the emissivity spectrum. For example, over water bodies, errors in emissivity of

up to 3% (0.03) have been found due to uncompensated atmospheric effects (Hulley and Hook 2009b; Tonooka and Palluconi 2005).

One method for improving the accuracy of the surface radiance product is to apply the WVS method (Tonooka 2005). Using 183 ASTER scenes over lakes, rivers, and sea surfaces, it was found that using the WVS method instead of the standard atmospheric correction improved estimates of surface temperature from 3 to 8 K in regions of high humidity (Tonooka 2005). These are substantial errors when considering that the required accuracy of the TES algorithm is ~1 K (Gillespie et al. 1998). This will also be demonstrated in the latter part of this document.

### **3 VIIRS and MODIS LST&E continuity**

LST data are acknowledged as a key Environmental Data Records (EDRs) by the NASA Earth Science Division, and an Essential Climate Variable (ECV) by the Global Climate Observing System (GCOS). As such, it is critical that LST data are produced with high accuracy and precision, but more importantly, that they are produced with consistent algorithms across different sensor platforms in order to maintain a continuous and well characterized data record. This is especially important for the VIIRS LST product on Suomi-NPP, which bridges the gap between NASA's EOS satellites and the next generation JPSS platforms. A long, stable record of LST is critical for monitoring climate trends, reducing systematic biases in land surface models, and is particularly useful for model evaluation in regions where few in situ measurements of surface air temperatures exist.

The current operational NOAA VIIRS LST EDR utilizes a split-window algorithm that relies on previously-generated emissivity dependent coefficients, and therefore does not produce a dynamically varying and multi-spectral land surface emissivity product. Furthermore, this algorithm deviates from the generalized split-window used in its MODIS counterpart (MOD11), resulting in a discontinuity in the current MODIS/VIIRS LST time series as previously reported by Guillevic et al. [18], who showed biases between the products of up to 4 K over arid regions and differences of up to 15 K for warm and moist atmospheric conditions. In addressing these issues, one of the main objectives of this study was to present an alternative physics-based algorithm (TES) for generation of the NASA VIIRS LST&E EDR in order to provide continuity with its MODIS TES counterpart (MOD21, Collection 6) [20].

As a demonstration of this, we show results of LST differences derived from two different approaches - the TES (present study) and the Split-Window (heritage) algorithms using MODIS Aqua/VIIRS Simultaneous Nadir Overpasses (SNOs) identified using the same matchup tool methodology as defined by Guillevic et al. [18]. Four months of data (Jan, Feb, and Aug Sep 2012) were used over the southwestern USA with a wide range of environmental conditions (temperatures from 260 - 340 K, precipitable water vapor from 0 - 5 cm), and including all land cover types identified in the IGBP classification.

Figure 11 shows LST differences between MODIS and VIIRS for the TES approach (top left), and split-window approaches (top right). Corresponding VIIRS retrieved LST and precipitable water vapor (PWV) extracted from MERRA-2 are also shown in the bottom panels. The LST differences between the VIIRS and MODIS TES approach are small and in general less than 0.5 K, with no dependence on environmental conditions or cover type, while the SW product differences are as high as 20 K over parts of the Sonoran and Mojave desert, for example. These large LST differences in the SW products are directly associated with high PWV and LST values as previously discussed in Guillevic et al. [18] which introduce large uncertainty in the VIIRS SW algorithm. This is because a single set of coefficients in the VIIRS SW algorithm are not able to capture and are not fully representative of extreme conditions such as these that introduce large nonlinearities in the Planck function.

Figure 12 shows histograms of LST differences between the VIIRS and MODIS products for a full set of 4 months of MODIS/VIIRS SNO's over CONUS during Jan, Feb, Aug, and Sep 2012, and show almost negligible bias (0.3 K) for the TES approach as opposed to a large positive bias in the SW approach (2 K). Larger differences of up to 3 K RMSE are found during the summer months (Aug, Sep) for the split-window products due to warmer and more humid conditions, while the TES results are unchanged. Discarding algorithmic differences, other sources of LST differences include view angle configuration differences, calibration, and differences in cloud masking between MODIS and VIIRS sensors.

Figure 13 shows VIIRS minus MODIS LST RMSE for the split-window algorithms and TES algorithm calculated from 4 months of MODIS and VIIRS SNO's over CONUS during Jan, Feb, Aug, and Sep 2012. LST differences were grouped according to standard IGBP classification. Note large differences in the split-window results especially for arid and semi-arid classes (shrublands, bare), while TES results are consistent and less than 1 K across all cover types.

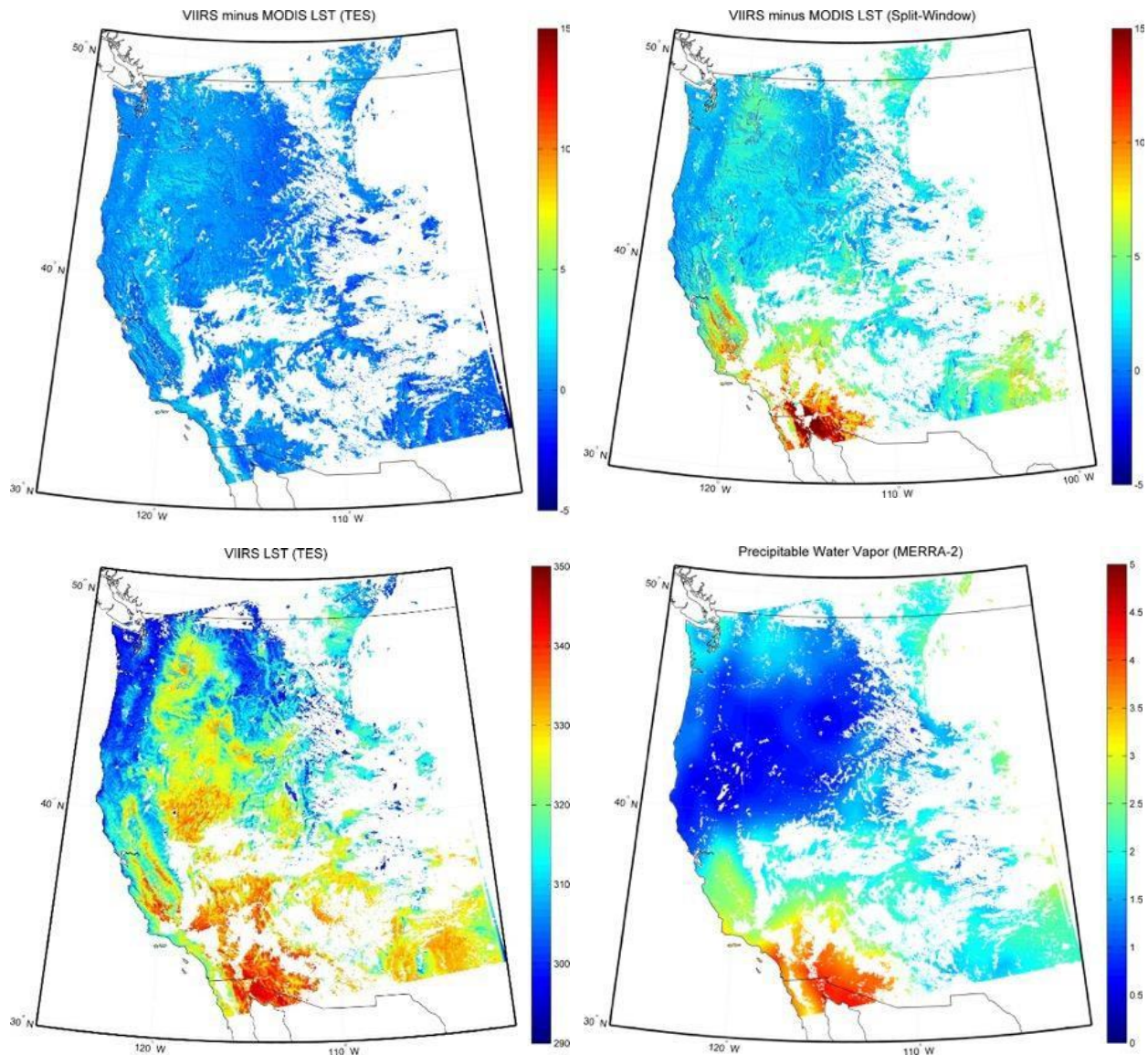


**Figure 11. Differences between the VIIRS and MODIS LST products in K using the TES algorithm (top left) and the split-window algorithm (top right). Corresponding VIIRS LST (bottom left) and MERRA-2 precipitable water vapor in cm (bottom right) are also shown. The granule overpass is on 11 August 2012 UTC 2040.**

Quantification of LST&E retrieval uncertainty was estimated using the Temperature Emissivity Uncertainty Simulator (TEUSim) developed by Hulley et al. [25]. TEUSim was developed to quantify the effects of algorithmic, atmospheric, and measurement uncertainties on the retrieval of LST and emissivity from a number of sensors including MODIS VIIRS, ASTER, and Landsat TIR data. The uncertainties are estimated with radiative transfer simulations

(MODTRAN 5.2) using 382 global radiosonde profiles [68] and 155 surface emissivity spectra [59] as input for a range of viewing angle configurations and surface temperatures for each profile. To estimate the total LST&E uncertainty a random error of 20% was assigned to the water vapor profiles, and 2 K to the air temperature profiles. The VIIRS IDPS split-window algorithm, MOD11 generalized split-window algorithm, and MODIS/VIIRS TES algorithm were then used to retrieve LST from the simulated radiances. Emissivity spectra were assigned according to IGBP to assign the appropriate coefficients for the split-window algorithms. Figure 14 shows LST differences between MODIS and VIIRS vs total column water vapor and LST for the split-window algorithms (top), and TES algorithm (bottom). Differences in formulation, coefficient generation, and emissivity assignment result in large differences between the current MODIS and VIIRS split-window LST products of up to 15 K for warm and humid conditions, while the TES algorithm differences are at the <0.5 K level since a consistent algorithm was used to retrieve LST&E from the 3 MODIS/VIIRS TIR bands.

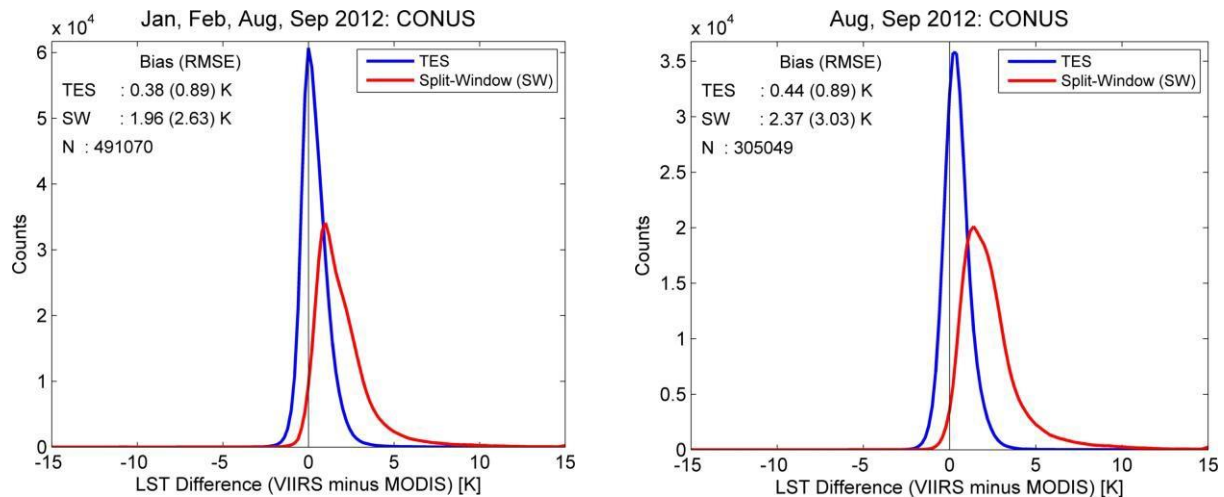


Figure 12. (Top) Histogram demonstrating the differences between VIIRS and MODIS LST products for all observations over continental USA (CONUS) during Jan, Feb, Aug, and Sep 2012 for two different algorithms: TES and split-window. The TES algorithm is currently used to produce the NASA LST&E products for MODIS and VIIRS (MOD21 and VNP21), while the split-window algorithm is used in the to produce the heritage MOD11 product(s) and the NOAA VLST product. (Bottom) same as above except only data for summer time (Aug, Sep).



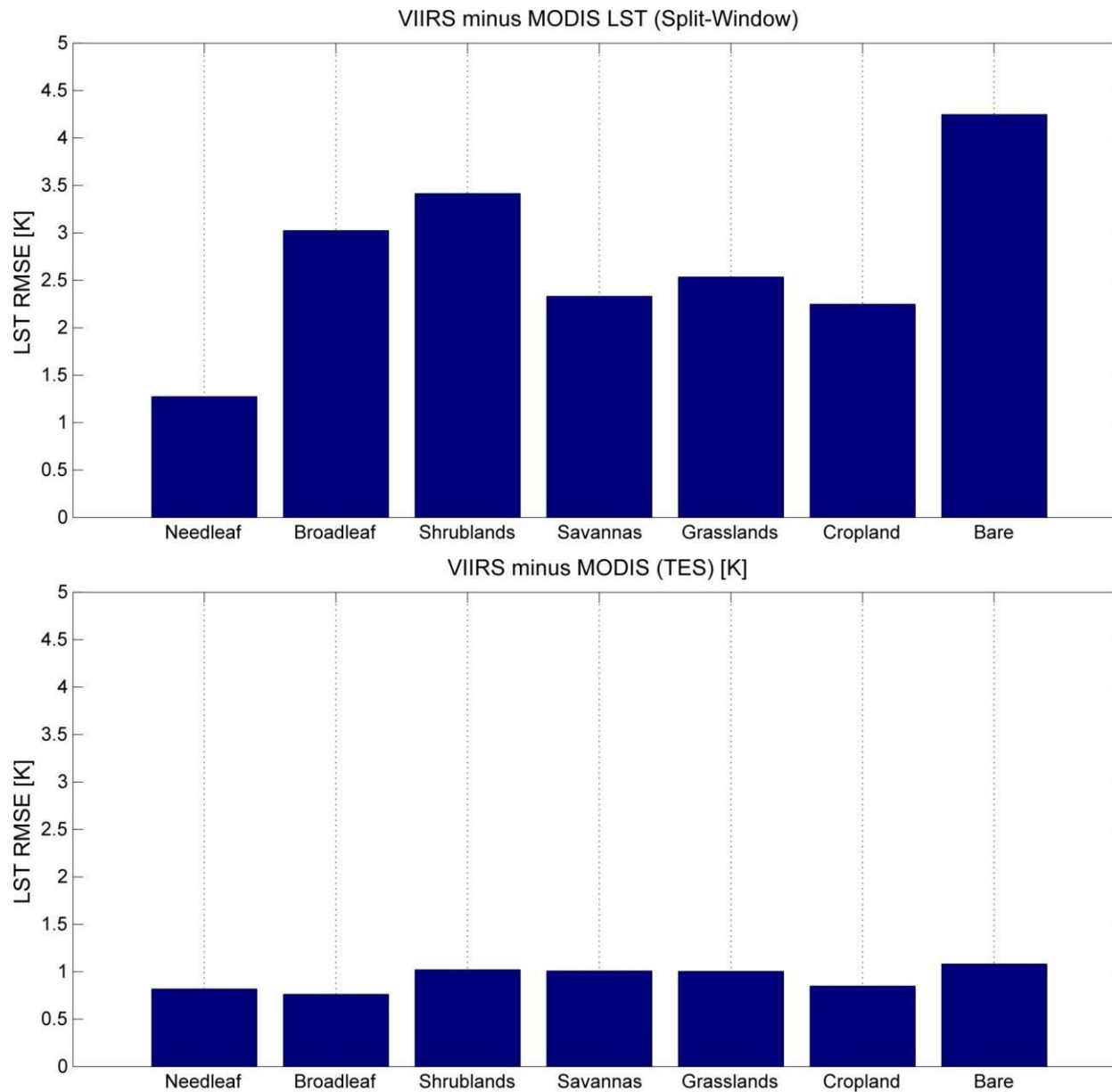


Figure 13. VIIRS minus MODIS LST RMSE for the split-window algorithms (top) and TES algorithm (bottom) calculated from 4 months of MODIS and VIIRS SNO's over CONUS during Jan, Feb, Aug, and Sep 2012. LST differences were grouped according to standard IGBP classification. Note large differences in the split-window results especially for arid and semi-arid classes (shrublands, bare), while TES results are consistent and less than 1 K across all cover types.

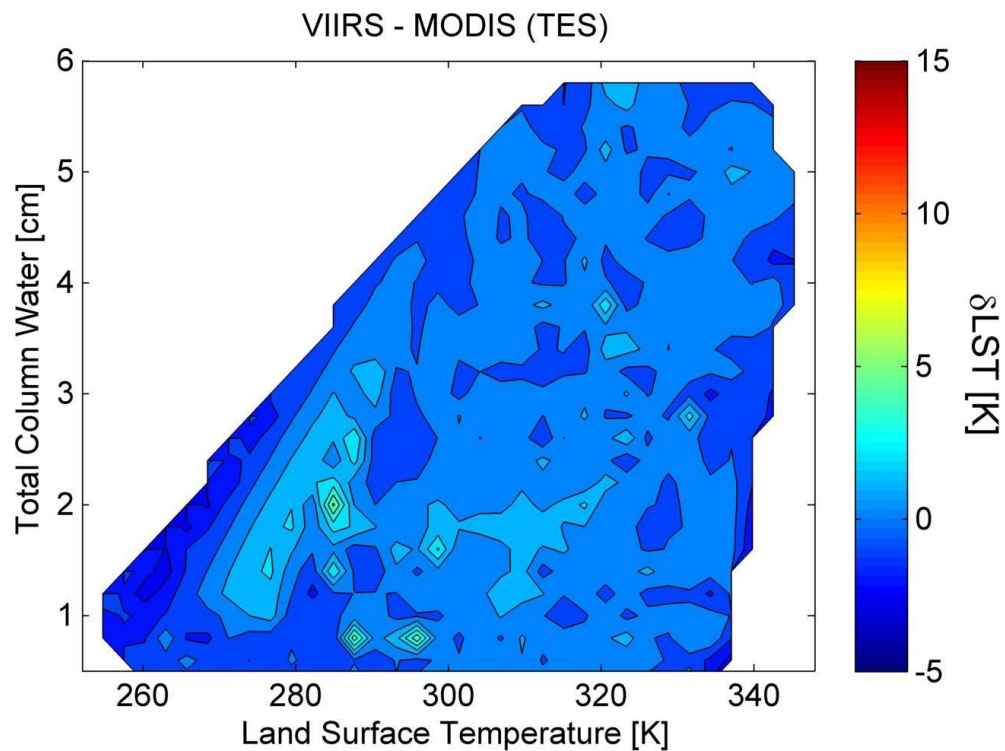
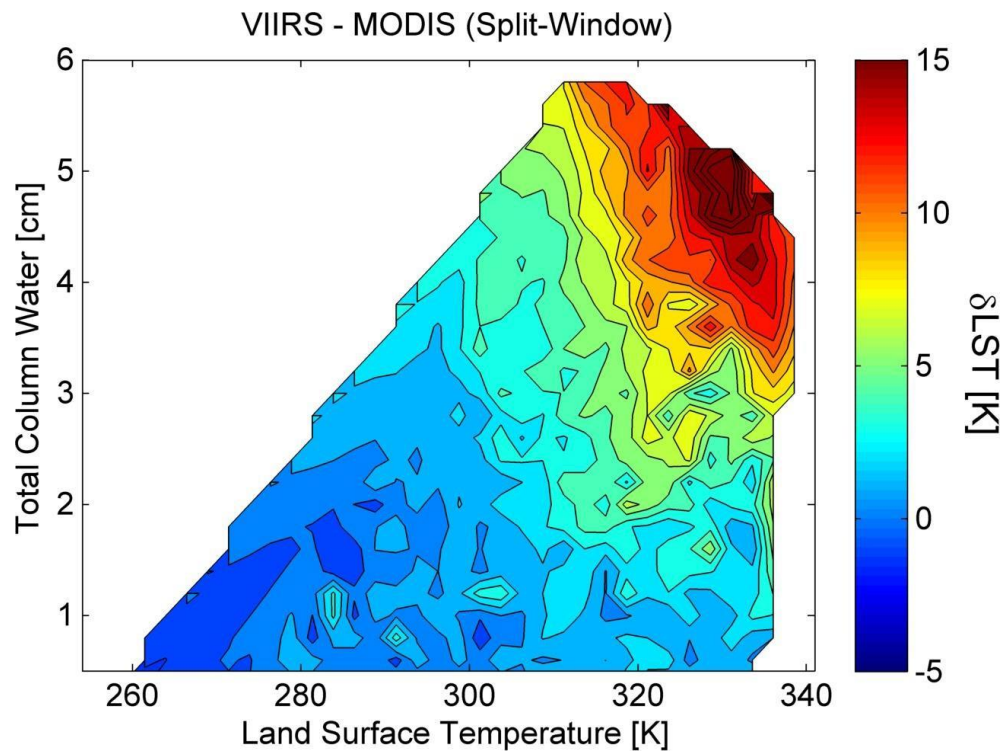


Figure 14. LST differences between MODIS and VIIRS vs total column water vapor and LST for the split-window algorithms (top), and TES algorithm (bottom). Differences in formulation, coefficient generation, and emissivity assignment result in large differences between the current MODIS and VIIRS split-window LST products.

## 4 Validation and Product Accuracy

Two methods have been established for validating VIIRS LST data: a conventional T-based method and an R-based method (Wan and Li 2008). The T-based method requires ground measurements over thermally homogenous sites concurrent with the satellite overpass, while the R-based method relies on a radiative closure simulation in a clear atmospheric window region to estimate the LST from top of atmosphere (TOA) observed brightness temperatures, assuming the emissivity is known from ground measurements. The T-based method is the preferred method, but it requires accurate in-situ measurements that are only available from a small number of thermally homogeneous sites concurrently with the satellite overpass. The R-based method is not a true validation in the classical sense, but it does not require simultaneous in-situ measurements and is therefore easier to implement both day and night over a larger number of global sites; however, it is susceptible to errors in the atmospheric correction and emissivity uncertainties. The MOD11\_L2 LST product has been validated with a combination of T-based and R-based methods over more than 19 types of thermally homogenous surfaces including lakes (Hook et al. 2007), dedicated field campaign sites over agricultural fields and forests (Coll et al. 2005), playas and grasslands (Wan et al. 2004; Wan 2008), and for a range of different seasons and years. LST errors are generally within  $\pm 1$  K for all sites under stable atmospheric conditions except semi-arid and arid areas, which had errors of up to 5 K (Wan and Li 2008).

Validation of emissivity data from space ideally requires a site that is homogeneous in emissivity at the scale of the imagery, allowing several image pixels to be validated over the target site. The nine sand dune validation sites chosen for the ASTER study and planned for use with the VNP21 product are: Great Sands National Park, Colorado; White Sands National Monument, New Mexico; Kelso Dunes, California; Algodones Dunes, California; Stovepipe Wells Dunes, California; Coral Pink Sand Dunes, Utah; Little Sahara Dunes, Utah; Killpecker Dunes, Wyoming; and Moses Lake Basalt Dunes, Washington. R-based validation of the VNP21 product is currently underway over these nine pseudo-invariant sites in southwestern United States, and the Lake Tahoe and Salton Sea cal/val sites.

Summarizing, for the VNP21 product we plan to use in-situ data from a variety of ground sites covering the majority of different land-cover types defined in the International Geosphere-

Biosphere Programme (IGBP). The sites will consist of water, vegetation (forest, grassland, and crops), and barren areas (Table 3).

**Table 3. The core set of global validation sites according to IGBP class to be used for validation and calibration of the VIIRS VNP21 land surface temperature and emissivity product.**

IGBP Class		Sites
0	Water	Tahoe, Salton Sea, CA
1,2	Needle-leaf forest	Krasnoyarsk, Russia; Tharandt, Germany; Fairhope, Alaska
3,4,5	Broad-leaf/mixed forest	Chang Baisan, China; Hainich, Germany; Hilo, Hawaii
6,7	Open/closed shrublands	Desert Rock, NV; Stovepipe Wells, CA
8,9,10	Savannas/Grasslands	Boulder, CO; Fort Peck, MT
12	Croplands	Bondville, IL; Penn State, PA; Sioux Falls, SD; Goodwin Creek, MS
16	Barren	Algodones Dunes, CA; Great Sands, CO; White Sands, NM; Kelso Dunes, CA; Namib Desert, Namibia; Kalahari Desert, Botswana

#### 4.1 Water Sites

For water surfaces, we will use the Lake Tahoe, California/Nevada, and Salton Sea, CA, automated validation sites where measurements of skin temperature have been made every two minutes and are used to validate the mid and thermal infrared data and products from ASTER and MODIS (Hook et al. 2007). Water targets are ideal for cal/val activities because they are thermally homogeneous and the emissivity is generally well known. A further advantage of Tahoe site is that the lake is located at high altitude, which minimizes atmospheric correction errors, and is large enough to validate sensors from pixel ranges of tens of meters to several kilometers.

Figure 15 shows emissivity spectra over the Salton Sea, showing the effects of applying the WVS atmospheric correction method on the shape of the emissivity spectrum when compared to using the standard (STD) correction method without WVS. The emissivity spectrum of water is high (~0.98) and flat and the results in Figure 11 show a dramatic improvement in emissivity accuracy in both magnitude (up to 0.06 for ASTER band 11, and 0.09 for MODIS band 29) and spectral shape when using the WVS as opposed to the STD method. Because of the humid day, where MOD07 precipitable water vapor (PWV) values were around 4 cm over the water, the spectral contrast of the STD emissivity results are overestimated for ASTER and MODIS data. However, when applying the WVS method, the ASTER emissivity spectra fall within 0.015 of the

lab-measured spectrum, while MODIS emissivity spectra are within 0.005 at all wavelengths. Differences between the 3- and 5-band TES algorithm applied to ASTER data were small.

Figure 16 shows the LST validation results for the two inland water validation sites using a total of 31 matched-up VIIRS overpasses in 2014. The results show that VNP21 LST retrievals are in good agreement with *in situ* radiometer LSTs at both sites with a mean bias of 0.50 K,  $R^2$  of 0.98 and RMSE of 1.41 K. In the figure, validation points for Lake Tahoe are shown with red points, and validation points for the Salton Sea site are shown with blue points. From the figure we can see that the Salton Sea site generally has higher lake temperatures (up to 307 K) than Lake Tahoe (less than ~295 K) for this set of observations.

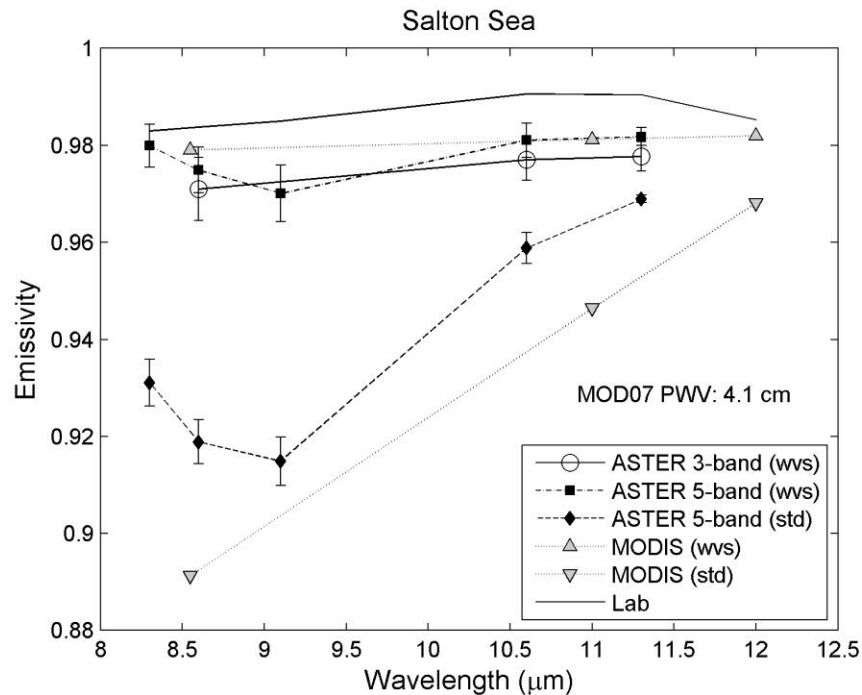
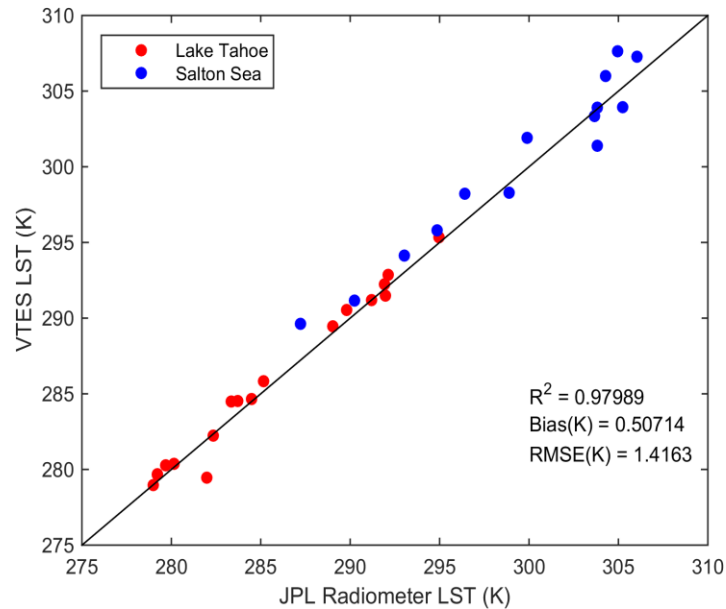


Figure 15. Emissivity spectra comparisons on June 15, 2000 over the Salton Sea between ASTER (3-band), ASTER (5-band), and MODTES, using the TES algorithm along with lab spectra of water from the ASTER spectral library. Results from the WVS method and the STD atmospheric correction are also shown. An estimate of the PWV from the MOD07 atmospheric product indicates very high humidity on this day.



**Figure 16. Scatterplot of VNP21 retrieved LST vs JPL radiometer LST at the inland water validation sites.**

## 4.2 Vegetated Sites

For vegetated surfaces (forest, grassland, savanna, and crops), we will use a combination of data from the Surface Radiation Budget Network (SURFRAD), FLUXNET, and NOAA-CRN sites. For SURFRAD, we will use a set of six sites established in 1993 for the continuous, long-term measurements of the surface radiation budget over the United States through the support of NOAA's Office of Global Programs (<http://www.srrb.noaa.gov/surfrad/>). The six sites (Bondville, IL; Boulder, CO; Fort Peck, MT; Goodwin Creek, MS; Penn State, PA; and Sioux Falls, SD) are situated in large, flat agricultural areas consisting of crops and grasslands and have previously been used to assess the MODIS and ASTER LST&E products with some success (Augustine et al. 2000; Wang and Liang 2009). From FLUXNET and the Carbon Europe Integrated Project (<http://www.carboeurope.org/>), we will include an additional four sites to cover the broadleaf and needleleaf forest biomes (e.g., Hainich and Tharandt, Germany; Chang Baisan, China; Krasnoyarsk, Russia), using data from the FLUXNET as well as data from the EOS Land Validation Core sites ([http://landval.gsfc.nasa.gov/coresite\\_gen.html](http://landval.gsfc.nasa.gov/coresite_gen.html)). Furthermore, the U.S. Climate Reference Network (USCRN) has been established to monitor present and future long-term climate data records (<http://www.ncdc.noaa.gov/crn/>). The network consists of 114 stations in the continental United States and is monitored by NOAA's National Climatic Data Center (NCDC). Initially, we plan to use the Fairhope, Alaska, and Hilo, Hawaii, sites from this network.

### 4.3 Pseudo-invariant Sand Dune Sites

For LST and emissivity validation over arid regions, we will use a set of nine pseudo-invariant, homogeneous sand dune sites in the southwestern United States (Hulley et al. 2009a) that were used for validating ASTER and MODIS products, and two sites over large sand dune seas in the Namib and Kalahari deserts in Southern Africa (Hulley et al. 2009b) used for validating AIRS. The emissivity and mineralogy of samples collected at these sites have been well characterized and are described by Hulley et al. (2009a).

Pseudo-invariant ground sites such as playas, salt flats, and claypans have been increasingly recognized as optimal targets for the long-term validation and calibration of visible, shortwave, and thermal infrared data (Bannari et al. 2005; Cosnefroy et al. 1996; de Vries et al. 2007; Teillet et al. 1998). We have found that large sand dune fields are particularly useful for the validation of TIR emissivity data (Hulley and Hook 2009a). Sand dunes have consistent and homogeneous mineralogy and physical properties over long time periods. They do not collect water for long periods as playas and pans might, and drying of the surface does not lead to cracks and fissures, typical in any site with a large clay component, which could raise the emissivity due to cavity radiation effects (Mushkin and Gillespie 2005). Furthermore, the mineralogy and composition of sand samples collected in the field can be accurately determined in the laboratory using reflectance and x-ray diffraction (XRD) measurements. In general, the dune sites should be spatially uniform and any temporal variability due to changes in soil moisture and vegetation cover should be minimal. Ideally, the surface should always be dry, since any water on the surface can increase the emissivity by up to 0.16 (16%) in the 8.2–9.2- $\mu\text{m}$  range depending on the type of soil (Mira et al. 2007).

#### 4.3.1 Emissivity Validation

Seasonal changes in vegetation cover, aeolian processes such as wind erosion, deposition and transport, and daily variations in surface soil moisture from precipitation, dew, and snowmelt are the primary factors that could potentially affect the temporal stability and spatial uniformity of the dune sites. Field observations during the spring and early summer of 2008 revealed that the major portion of the dune sites was bare, with the exception of Kelso and Little Sahara, which contained sparse desert grasses and reeds on the outer perimeter of the dune field and in some interdunal areas. Nonetheless, this does not mean the other seven dune sites did not have vegetation

in the past, since 2000. The presence of soil moisture would result in a significant increase in TIR emissivity at the dune sites, caused by the water film on the sand particles decreasing its reflectivity (Mira et al. 2007; Ogawa et al. 2006), particularly for VIIRS band M14 in the quartz Reststrahlen band. However, given that the majority of dune validation sites are aeolian (high winds), at high altitude (low humidity), and in semi-arid regions (high skin temperatures), the lifetime of soil moisture in the first few micrometers of the surface skin layer as measured in the TIR is most likely small due to large sensible heat fluxes and, therefore, high evaporation rates, in addition to rapid infiltration. Consequently, we hypothesize that it would most likely take a very recent precipitation event to have any noticeable effect on remote-sensing observations of TIR emissivity over these types of areas.

Figure 17 shows emissivity spectra from sand dune samples collected at ten sand dune sites in the southwestern United States. The spectra cover a wide range of emissivities in the TIR region. These sites will be the core sites used to validate the emissivity (as well as LST) products from VIIRS.

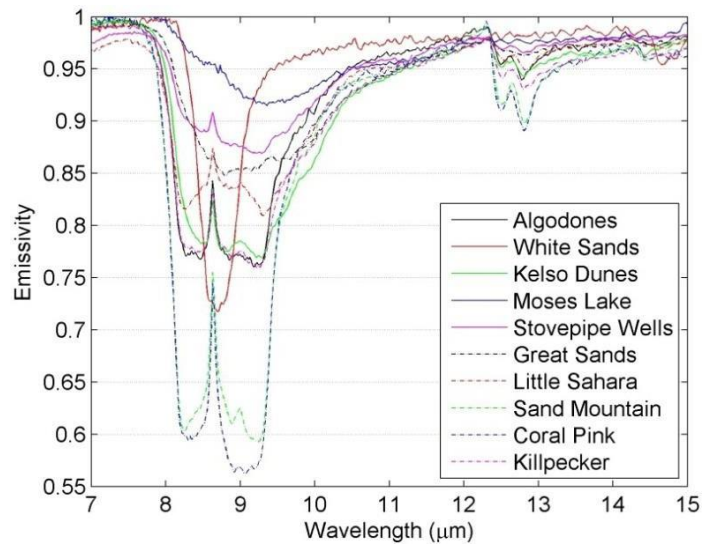


**Figure 17. Laboratory-measured emissivity spectra of sand samples collected at ten pseudo-invariant sand dune validation sites in the southwestern United States. The sites cover a wide range of emissivities in the TIR region.**



#### 4.3.2 *Emissivity comparison with ASTER GED*

For the assessment of the VNP21 retrieved emissivity product, we inter-compare the VNP21 retrievals with emissivity spectra derived from ASTER GEDv3 (Hulley et al. 2015). The ASTER GED is a global emissivity dataset developed using millions of cloud free ASTER retrieved emissivity data over a 9-year period (2000-2008), and aggregated and mosaicked to produce a gridded global map. Recently, version 3 of the dataset has been made available that provides an average surface emissivity at the five ASTER TIR wavelengths (8.3, 8.6, 9.1, 10.6, and 11.3  $\mu\text{m}$ ) and in two different resolutions - 3 arc sec ( $\sim 100$  m) and 30 arc sec ( $\sim 1$  km). ASTER GEDv3 has been extensively validated in the past over mostly arid and semi-arid regions with an average absolute band error of  $\sim 1\%$  (Hulley et al. 2015; Hulley et al. 2009a).

Figure 18 shows a comparison between ASTER GED emissivity and emissivity retrieved from the VNP21 algorithm at the band M14 for a VIIRS granule over the southwestern USA on 19 June 2014 UTC 2050. As shown in this figure, the entire region is spatially heterogeneous with emissivities ranging from 0.7 over quartz sands of the Algodones dunes to near 1 over water targets such as the Salton Sea and dense vegetation. Overall, the spatial patterns of emissivity variability between the ASTER GED and VNP21 retrieved emissivity compare well. The corresponding emissivity difference image and histogram plot showing the differences between the two emissivity fields (VNP21 – ASTER GED) are shown in the bottom panels of the figure. The emissivity difference histogram has a uni-modal peak with mean and standard deviation of 0.008 and 0.012, respectively. The  $\sim 1\%$  bias is within the uncertainty estimated from the ASTER adjustment method, and the retrieval accuracy of the TES algorithm. Note that, a few granules were selected in each month for comparison so that the comparisons were not biased towards a particular season, or temperature range. The mean difference between VNP21 and ASTER GED for each band is negligible and at the 0.1% level (RMSE =  $\sim 0.01$ ). This highlights the consistency between the VNP21 and ASTER GED emissivity spectra for the three TIR bands.

Figure 19 shows a comparison between VNP21 retrieved emissivity and corresponding ASTER GED v3 emissivity spectra. A total of 30 collocation samples during 2014 have been made available for the inter-comparison in clear-sky conditions at each site. At least two cloud free samples were selected from every month in the year for the comparison. Figure 19 shows a comparison between the mean emissivity spectra for the three VIIRS TIR bands and corresponding emissivity spectra from the ASTER GED at the sand dunes sites. The error bars

represent the temporal variability of the emissivity values. The original five band ASTER GED emissivity spectra were spectrally adjusted to the three VIIRS TIR bands as described earlier. In general, there is a very good agreement in the spectral shape and absolute value between the VNP21 retrieval and the ASTER GED adjusted emissivity spectra at the four assessment sites with mean differences ranging from 0.01-0.02 in band M14 (8.55  $\mu\text{m}$ ). The mean emissivity differences between the VNP21 and the ASTER GED for band M15 (10.76  $\mu\text{m}$ ) and M16 (12.01  $\mu\text{m}$ ), are less than 0.01.

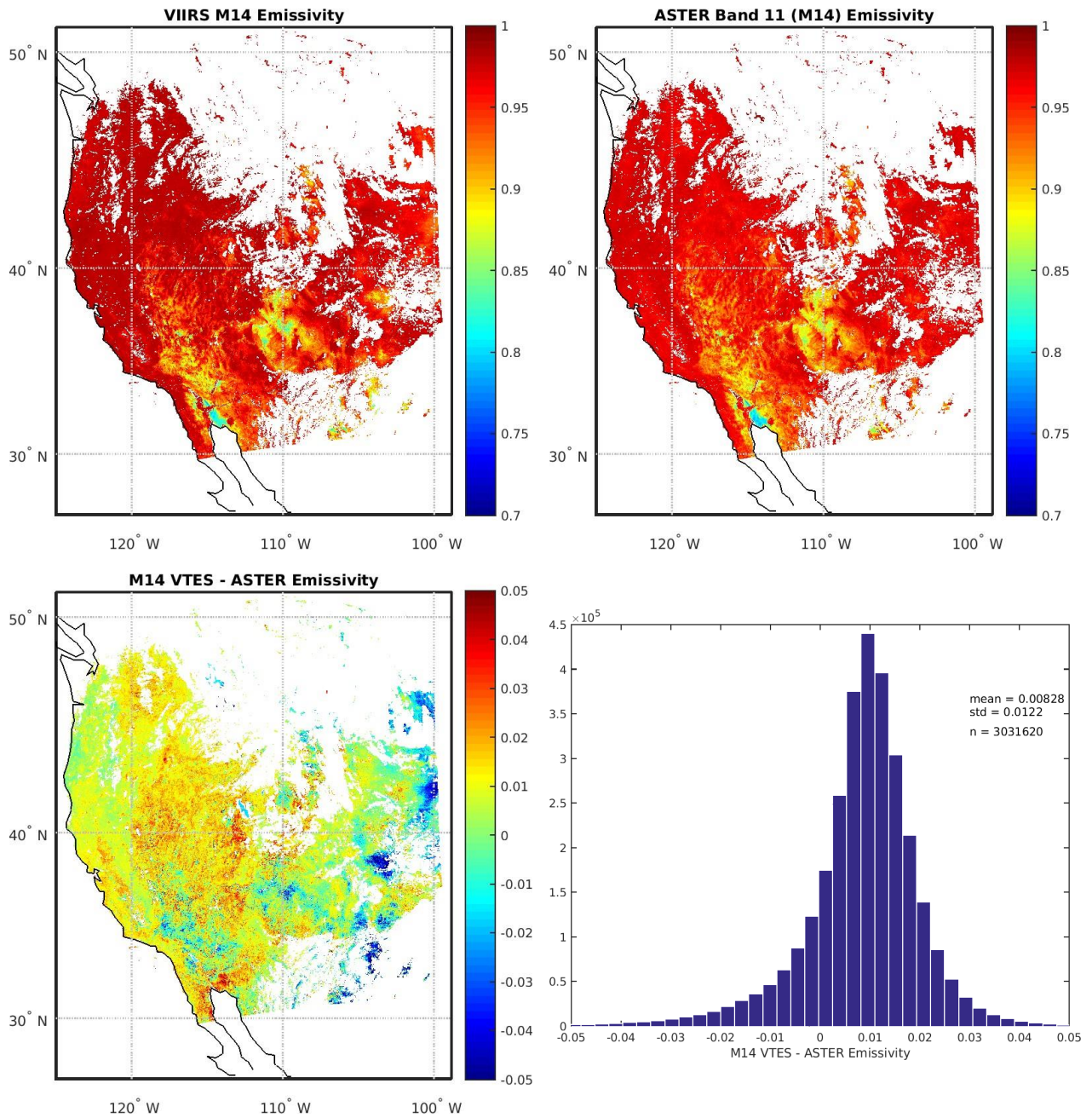


Figure 18. The emissivity maps from the VNP21 retrieval (top left) and the ASTER GED (top right) at the VIIRS band M14 (8.55  $\mu\text{m}$ ). Corresponding emissivity difference map (bottom left) and the histogram of their differences (bottom right) are also shown. The ASTER GED emissivity is adjusted to the VIIRS M14 band ( $\sim 8.55 \mu\text{m}$ ) for comparison. The granule overpass is on 19 June 2014 UTC 2050.

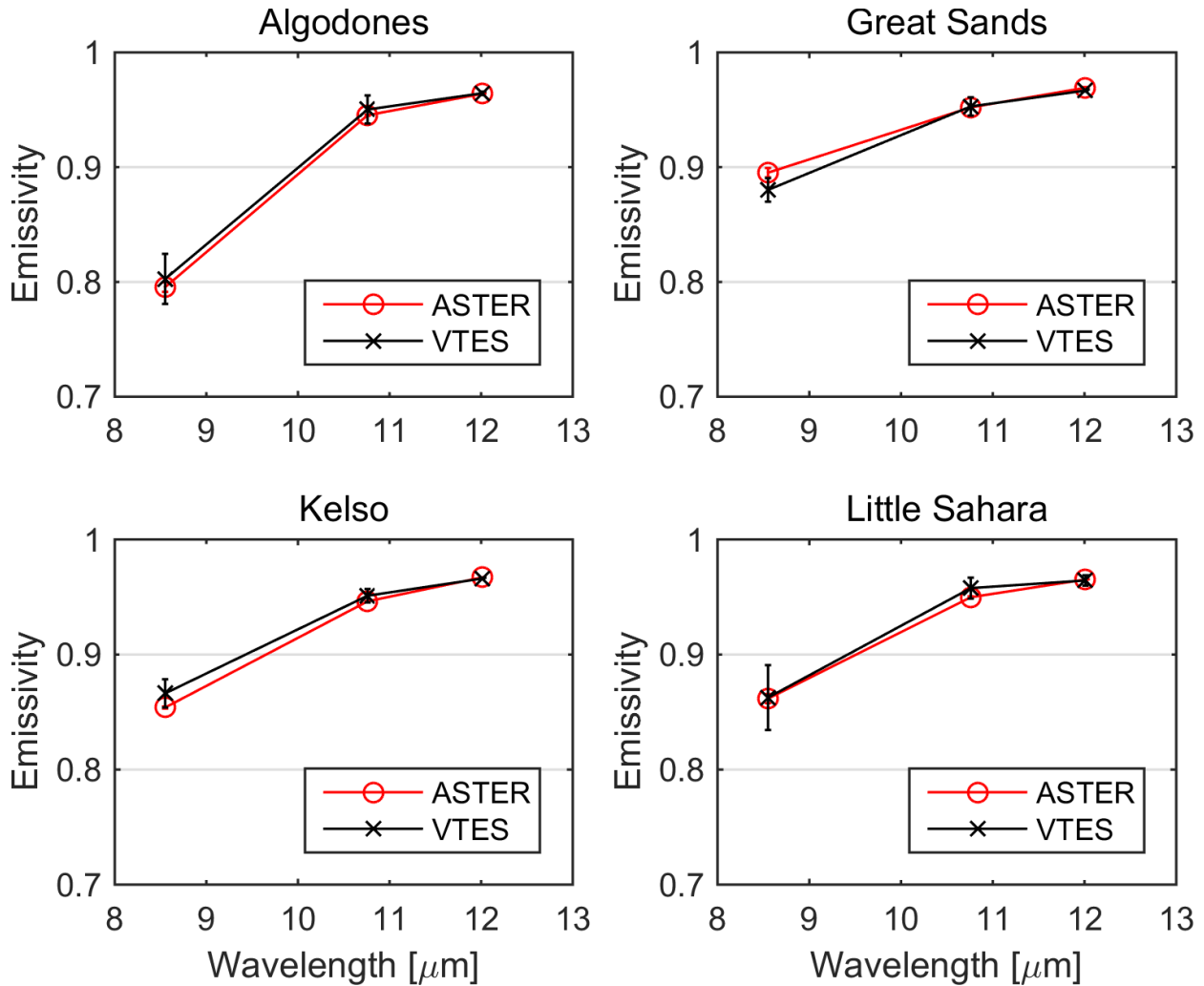


Figure 19. Emissivity spectra comparison between VNP21 retrieved emissivity and the ASTER GED v3 emissivities that were spectrally and spatially adjusted to match VIIRS at 4 pseudo-invariant sand dune sites.

#### 4.3.3 LST Validation

For LST validation over the sand dune sites, we will use a recently established R-based validation method (Coll et al. 2009b; Wan and Li 2008). The advantage of this method is that it does not require in-situ measurements, but instead relies on atmospheric profiles of temperature and water vapor over the site and an accurate estimation of the emissivity. The R-based method is based on a ‘radiative closure simulation’ with input surface emissivity spectra from either lab or field measurements, atmospheric profiles from an external source (e.g., model or radiosonde), and the retrieved LST product as input. A radiative transfer model is used to forward model these parameters to simulate at-sensor BTs in a clear window region of the atmosphere (11–12  $\mu\text{m}$ ). The

input LST product is then adjusted in 2-K steps until two calculated at-sensor BTs bracket the observed BT value. An estimate of the ‘true’ temperature (  $LST_{R-based}$  ) is then found by interpolation between the two calculated BTs, the observed BT, and the initial retrieved LST used in the simulation. The LST error, or uncertainty in the LST retrieval is simply found by taking the difference between the retrieved LST product and the estimate of  $LST_{R-based}$ . This method has been successfully applied to MODIS LST products in previous studies (Coll et al. 2009a; Wan and Li 2008; Wan 2008). For VIIRS data, band M15 (10.78–11.28  $\mu\text{m}$ ) is typically used for the simulation since it is the least sensitive to atmospheric absorption in the longwave region. The advantage of the R-based method is that it can be applied to a large number of global sites where the emissivity is known (e.g., from field measurements) and during night- and daytime observations to define the diurnal temperature range.

The archive of all North American VIIRS data, as defined by the bounding box 22° to 71° N and 55° to 169° W, is used in this process for each pseudo-invariant site. Each scene is tested to see if it contained the location of interest. Scenes that did not contain the point of interest were eliminated, as were scenes in which the point was located either along scene margins (the first or last row or column of pixels) or whose viewing angle exceeded 40°. Finally, scenes in which the pixel of interest was cloudy, or had greater than three neighboring pixels that were cloudy, were eliminated. Any scene remaining at this point was used for determination of LST. LST data were derived either directly from the VLST product or calculated locally using the algorithm for the VNP21 product. Following LST retrieval, atmospheric profiles over the pseudo-invariant site were obtained from either the MERRA model. Together with the original land surface temperature from VLST, these values were then used as input to RTTOV to calculate the Top Of Atmosphere Radiance.

Wan and Li (2008) proposed a quality check to assess the suitability of the atmospheric profiles by looking at differences between observed and calculated BTs in two nearby window regions with different absorption features. For example, the quality check for VIIRS bands M14 and M15 at 11 and 12  $\mu\text{m}$  is:

$$\delta(T_{11} - T_{12}) = (T_{11}^{obs} - T_{12}^{obs}) - (T_{11}^{calc} - T_{12}^{calc}) \quad (19)$$

where:  $T_{11}^{obs}$  and  $T_{12}^{obs}$  are the observed brightness temperatures at 11 and 12  $\mu\text{m}$  respectively, and  $T_{11}^{calc}$  and  $T_{12}^{calc}$  are the calculated brightness temperatures from the R-based simulation at 11 and 12  $\mu\text{m}$  respectively. If  $\delta(T_{11} - T_{12})$  is close to zero, then the assumption is that the atmospheric

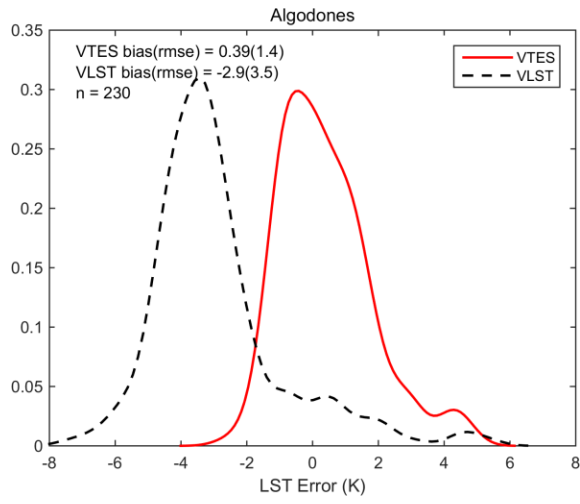
temperature and water vapor profiles are accurately representing the true atmospheric conditions at the time of the observation, granted the emissivity is already well known. Because water vapor absorption is higher in the 12- $\mu\text{m}$  region, negative residual values of  $\delta(T_{11} - T_{12})$  imply the R-based profiles are overestimating the atmospheric effect, while positive values imply an underestimation of atmospheric effects. A simple threshold can be applied to filter out any unsuitable candidate profiles for validation ( $\pm 0.5$  K)

Figure 20 shows error histograms of VIIRS retrieved LST for NASA VNP21 (red) and NOAA VLST (black dashed) using the R-based LST as truth for three pseudo-invariant sites and 2 vegetated sites using all clear-sky VIIRS overpasses from 2012-2015. The results show that the VLST split-window algorithm underestimates the LST with a cold bias of 3–5 K at all bare sites while VNP21 biases are at the  $<1.5$  K level, with lower RMSE's. The reason for the VLST cold bias is that the emissivity for barren surfaces is assigned one value that is fixed ( $\sim 0.96$  for M15 band). This causes large LST errors over bare sites where the mineralogy results in emissivities lower than that fixed value. The VNP21 algorithm, on the other hand, physically retrieves the spectral emissivity for the three VIIRS TIR bands along with the LST, and this results in more accurate LST results, particularly over bare regions where emissivity variations can be large, both spatially and spectrally. The results at the two vegetated sites (Texas Grass, Redwood) are similar for both products with negligible bias and RMSE's at the 1 K level. Table 4 shows a summary of the LST validation statistics at the five sites.

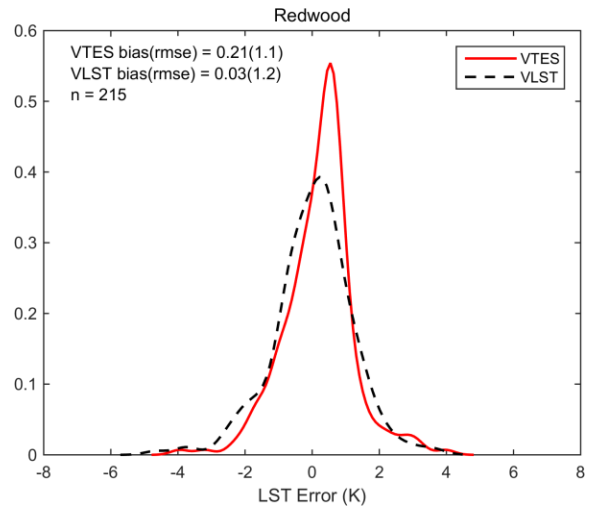
**Table 4. R-based LST validation statistics from three pseudo-invariant sand dune sites and two vegetated sites using all VNP21 and VLST LST retrievals from 2012-2015.**

	VNP21 Bias (K)	VLST Bias (K)	VNP21 RMSE (K)	VLST RMSE (K)
Algodones dunes	0.39	-2.9	1.4	3.5
Kelso	-1.5	1.9	1.9	4.8
Little Sahara	-1.21	3.9	1.5	4.1
Redwood National Park	0.21	0.03	1.1	1.2
Texas Grassland	-0.23	-0.29	1.1	1.4

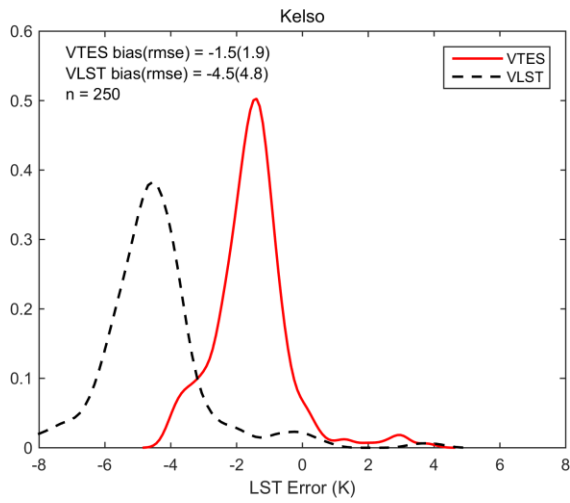
### A) Algodones dunes



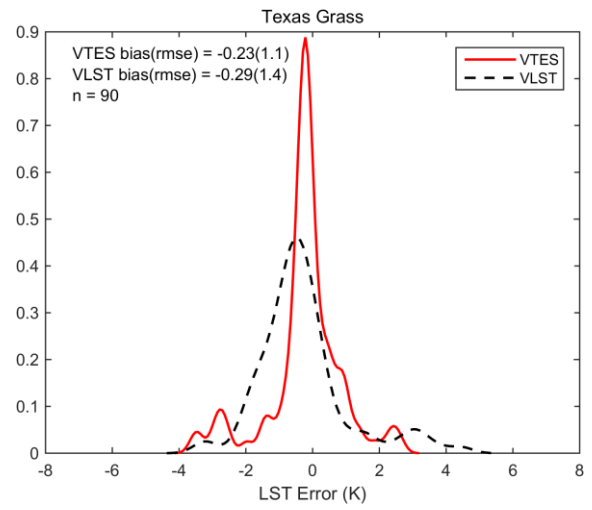
### B) Redwood National Park



### C) Kelso dunes



### D) Texas Grassland



### E) Little Sahara

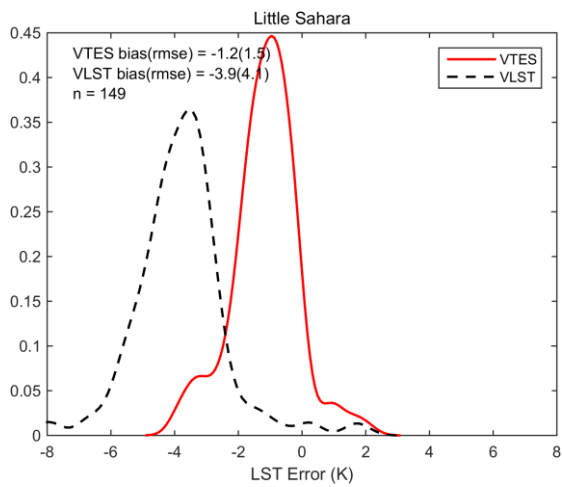


Figure 20. An example of the R-based LST validation method applied to the VNP21 (VTES) and NOAA VLST LST products over 3 pseudo-invariant sand dune sites (Algodones, Kelso, Little Sahara) and two vegetated sites (Redwood, Texas Grass) using all data during 2012. NCEP profiles and lab-measured emissivities from samples collected at the sites were used for the R-based calculations.

## 5 Data Formats

### 5.1 Format

VNP21 data will be available in Netcdf/HDF5 Scientific Data Sets (SDSs) format with output variables summarized in Table 5.

Table 5. The Scientific Data Sets (SDSs) in the VNP21 product.

SDS	Long Name	Data type	Units	Valid Range	Fill Value	Scale Factor	Offset
LST	Land Surface Temperature	uint16	K	7500-65535	0	0.02	0.0
QC	Quality control for LST and emissivity	uint16	n/a	0-65535	0	n/a	n/a
Emis_M14	Band M14 emissivity	uint8	n/a	1-255	0	0.002	0.49
Emis_M15	Band M15 emissivity	uint8	n/a	1-255	0	0.002	0.49
Emis_M16	Band M16 emissivity	uint8	n/a	1-255	0	0.002	0.49
LST_err	Land Surface Temperature error	uint8	K	1-255	0	0.04	0.0
Emis_M14_err	Band M14 emissivity error	uint16	n/a	0-65535	0	0.0001	0.0
Emis_M15_err	Band M15 emissivity error	uint16	n/a	0-65535	0	0.0001	0.0
Emis_M16_err	Band M16 emissivity error	uint16	n/a	0-65535	0	0.0001	0.0
View_angle	VIIRS view angle for current pixel	uint8	Deg	0-180	0	0.5	0.0
NDVI	Normalized Difference Vegetation Index	uint16	n/a	0-65535	0	0.0001	0.0
PWV	Precipitable Water Vapor	uint16	cm	0-65535	0	0.001	0.0
Oceanpix	Ocean-land mask	uint8	n/a	1-255	0	n/a	n/a



## 5.2 QA Metadata

The T and  $\epsilon$  products will need to be assessed using a set of quality control (QC) flags. These QC flags will involve automatic tests processed internally for each pixel and will depend on various retrieval conditions such as whether the pixel is over land or ocean surface, the atmospheric water vapor content (dry, moist, very humid, etc.), and cloud cover. The data quality attributes will be set automatically according to parameters set on data conditions during algorithm processing and will be assigned as either “good”, “unreliable,” or “bad.” Quality. Estimates of the accuracy and precision of the T and  $\epsilon$  product will be reported in a separate data plane. At each step in the TES algorithm, a variety of performance information will be output, which will give the user a summary of algorithm statistics in a spatial context. This type of information will be useful for determining surface type, atmospheric conditions, and overall performance of TES.

The architecture of the VIIRS T and  $\epsilon$  QA data plane will closely resemble that of the MOD21 product. A value of 0 in the QC bit flags means good, cloud free data quality and no further analysis of the QC bits is necessary. Users may use data of 'unreliable quality' (bits 1&0 = 01), but caution should be taken since either the retrieved emissivity is suspect (emissivity in both longwave bands M14 and M15 < 0.95 indicating possible cloud), the pixel is within 2 pixels of nearby detected cloud, the pixel had transmissivity less than 0.4 indicating possible cloud or high humidity resulting in higher uncertainty in the TES retrieval. A value of 11 for bits 1&0 indicates that the pixel was not produced due to it being an ocean pixel, poorly calibrated radiance data based on the L1B uncertainty index flag, or the TES algorithm failed to converge (usually due to undetected cloud, but rare). It will consist of header information followed by a 16-bit QA data plane. The structure of the QA data plane will consist of the following primary fields, which are detailed in Table 6:

1. Mandatory QA flags describing if the data is produced or not, quality, and cloud.
2. Data quality: Good, missing, fairly or poorly calibrated.
3. Cloud Flag: Cloud mask characteristics
4. Number of iterations needed to remove reflected downwelling sky irradiance.
5. Atmospheric opacity test for humid scenes, using  $L_{\lambda}^{\downarrow}/L'$  test.
6. MMD regime: MMD < 0.3 (near-graybody) or MMD > 0.3 (likely bare).
7. Estimated emissivity accuracy

8. Estimated LST accuracy

**Table 6. Bit flags defined in the QC\_Day and QC\_Night SDS in the VNP21A2 product. (Note: Bit 0 is the least significant bit).**

Bits	Long Name	Description
1&0	Mandatory QA flags	<p>00 = Pixel produced, good quality, no further QA info necessary</p> <p>01 = Pixel produced but unreliable quality. Either one or more of the following conditions are met: emissivity in both bands 14 and 15 &lt; 0.95, retrieval affected by nearby cloud, low transmissivity due to high water vapor loading (&lt;0.4). Recommend more detailed analysis of other QC information</p> <p>10 = Pixel not produced due to cloud</p> <p>11 = Pixel not produced due to reasons other than cloud (e.g. ocean pixel, poorly calibrated input radiance, TES algorithm divergence flag)</p>
3 & 2	Data quality flag	<p>00 = Good data quality of L1B bands 29, 31, 32</p> <p>01 = Missing pixel</p> <p>10 = Fairly calibrated</p> <p>11 = Poorly calibrated, TES processing skipped</p>
5 & 4	Cloud flag	<p>00 = Cloud free pixel</p> <p>01 = Thin cirrus</p> <p>10 = Pixel within 2 pixels of nearest cloud (~2km)</p> <p>11 = Cloud pixel</p>
7 & 6	TES Iterations (k)	<p>00 = <math>\geq 7</math> (Slow convergence)</p> <p>01 = 6 (Nominal)</p> <p>10 = 5 (Nominal)</p> <p>11 = <math>&lt; 5</math> (Fast)</p>
9 & 8	Atmospheric Opacity $L_{\lambda}^{\downarrow}/L'$	<p>00 = <math>\geq 0.3</math> (Warm, humid air; or cold land)</p> <p>01 = 0.2 - 0.3 (Nominal value)</p>

		<p>10 = 0.1 - 0.2 (Nominal value)</p> <p>11 = &lt;0.1 (Dry, or high altitude pixel)</p>
11 & 10	<p>Min-Max Difference (MMD). Difference between minimum and maximum emissivity for bands M14, M15, M16</p>	<p>00 = &gt;0.15 (Most silicate rocks)</p> <p>01 = 0.1 - 0.15 (Rocks, sand, some soils)</p> <p>10 = 0.03 - 0.1 (Mostly soils, mixed pixel)</p> <p>11 = &lt;0.03 (Vegetation, snow, water, ice)</p>
13 & 12	<p>Emissivity accuracy</p>	<p>00 = &gt;0.017 (Poor performance)</p> <p>01 = 0.015 - 0.017 (Marginal performance)</p> <p>10 = 0.013 - 0.015 (Good performance)</p> <p>11 = &lt;0.013 (Excellent performance)</p>
15 & 14	<p>LST accuracy</p>	<p>00 = &gt;2.5 K (Poor performance)</p> <p>01 = 1.5 - 2.5 K (Marginal performance)</p> <p>10 = 1 - 1.5 K (Good performance)</p> <p>11 = &lt;1 K (Excellent performance)</p>

## 6 References

- Abdalati, W., & Steffen, K. (2001). Greenland ice sheet melt extent: 1979-1999. *Journal of Geophysical Research-Atmospheres*, *106*, 33983-33988
- Anderson, M.C., Hain, C.R., Wardlow, B., Mecikalski, J.R., & Kustas, W.P. (2011a). Evaluation of a drought index based on thermal remote sensing of evapotranspiration over the continental U.S. *Journal of Climate*, *24*, 2025-2044
- Anderson, M.C., Kustas, W.P., Norman, J.M., Hain, C.R., Mecikalski, J.R., Schultz, L., Gonzalez-Dugo, M.P., Cammalleri, C., d'Urso, G., Pimstein, A., & Gao, F. (2011b). Mapping daily evapotranspiration at field to continental scales using geostationary and polar orbiting satellite imagery. *Hydrology and Earth System Sciences*, *15*, 223-239
- Anderson, M.C., Norman, J.M., Mecikalski, J.R., Otkin, J.A., & Kustas, W.P. (2007). A climatological study of evapotranspiration and moisture stress across the continental United States based on thermal remote sensing: 2. Surface moisture climatology. *Journal of Geophysical Research-Atmospheres*, *112*
- Augustine, J.A., DeLuise, J.J., & Long, C.N. (2000). SURFRAD - A national surface radiation budget network for atmospheric research. *Bulletin of the American Meteorological Society*, *81*, 2341-2357
- Baldrige, A.M., Hook, S.J., Grove, C.I., & Rivera, G. (2009). The ASTER Spectral Library Version 2.0. *Remote Sensing of Environment*, *114*, 711-715
- Bannari, A., Omari, K., Teillet, R.A., & Fedosejevs, G. (2005). Potential of getis statistics to characterize the radiometric uniformity and stability of test sites used for the calibration of earth observation sensors. *IEEE Transactions on Geoscience and Remote Sensing*, *43*, 2918-2926
- Benson, C.S. (1996). Stratigraphic studies in the snow and firn of the Greenland ice sheet, Snow, Ice and Permafrost Research Establishment (now U.S. Army Cold Regions Research and Engineering Laboratory). In
- Bonan, G.B., Oleson, K.W., Vertenstein, M., Levis, S., Zeng, X.B., Dai, Y.J., Dickinson, R.E., & Yang, Z.L. (2002). The land surface climatology of the community land model coupled to the NCAR community climate model. *Journal of Climate*, *15*, 3123-3149
- Bosilovich, M.G., Chen, J.Y., Robertson, F.R., & Adler, R.F. (2008). Evaluation of global precipitation in reanalyses. *Journal of Applied Meteorology and Climatology*, *47*, 2279-2299
- Chevallier, F. (2000). Sampled database of 60-level atmospheric profiles from the ECMWF analyses. In
- Coll, C., Caselles, V., Galve, J.M., Valor, E., Niclos, R., Sanchez, J.M., & Rivas, R. (2005). Ground measurements for the validation of land surface temperatures derived from AATSR and MODIS data. *Remote Sensing of Environment*, *97*, 288-300
- Coll, C., Caselles, V., Valor, E., Niclos, R., Sanchez, J.M., Galve, J.M., & Mira, M. (2007). Temperature and emissivity separation from ASTER data for low spectral contrast surfaces. *Remote Sensing of Environment*, *110*, 162-175
- Coll, C., Wan, Z.M., & Galve, J.M. (2009a). Temperature-based and radiance-based validations of the V5 MODIS land surface temperature product. *Journal of Geophysical Research-Atmospheres*, *114*, D20102, doi:20110.21029/22009JD012038
- Coll, C., Wan, Z.M., & Galve, J.M. (2009b). Temperature-based and radiance-based validations of the V5 MODIS land surface temperature product. *Journal of Geophysical Research-Atmospheres*, *114*, -
- Comiso, J.C. (2006). Arctic warming signals from satellite observations. *Weather* *61*, 70-76

Cosnefroy, H.N., Leroy, M., & Briottet, X. (1996). Selection and characterization of Saharan and Arabian desert sites for the calibration of optical satellite sensors. *Remote Sensing of Environment*, 58, 101-114

de Vries, C., Danaher, T., Denham, R., Scarth, P., & Phinn, S. (2007). An operational radiometric calibration procedure for the Landsat sensors based on pseudo-invariant target sites. *Remote Sensing of Environment*, 107, 414-429

Eyre, J.R., & Woolf, H.M. (1988). Transmittance of Atmospheric Gases in the Microwave Region - a Fast Model. *Applied Optics*, 27, 3244-3249

Francois, C., & Otle, C. (1996). Atmospheric corrections in the thermal infrared: Global and water vapor dependent Split-Window algorithms - Applications to ATSR and AVHRR data. *Ieee Transactions on Geoscience and Remote Sensing*, 34, 457-470

French, A.N., & Inamdar, A. (2010). Land cover characterization for hydrological modelling using thermal infrared emissivities. *International Journal of Remote Sensing*, 31, 3867-3883

French, A.N., Schmugge, T.J., Ritchie, J.C., Hsu, A., Jacob, F., & Ogawa, K. (2008). Detecting land cover change at the Jornada Experimental Range, New Mexico with ASTER emissivities. *Remote Sensing of Environment*, 112, 1730-1748

Gillespie, A., Rokugawa, S., Hook, S., Matsunaga, T., & Kahle, A.B. (1999). Temperature/Emissivity Separation Algorithm Theoretical Basis Document, Version 2.4, ASTER TES ATBD, NASA Contract NAS5-31372, 31322 March, 31999

Gillespie, A., Rokugawa, S., Matsunaga, T., Cothorn, J.S., Hook, S., & Kahle, A.B. (1998). A temperature and emissivity separation algorithm for Advanced Spaceborne Thermal Emission and Reflection Radiometer (ASTER) images. *IEEE Transactions on Geoscience and Remote Sensing*, 36, 1113-1126

Gottsche, F.M., & Hulley, G.C. (2012). Validation of six satellite-retrieved land surface emissivity products over two land cover types in a hyper-arid region. *Remote Sensing of Environment*, 124, 149-158

Gustafson, W.T., Gillespie, A.R., & Yamada, G.J. (2006). Revisions to the ASTER temperature/emissivity separation algorithm. In *2nd International Symposium on Recent Advances in Quantitative Remote Sensing*. Torrent (Valencia), Spain

Hall, D.K., Williams Jr., R.S., Casey, K.A., Digirolamo, N.E., & Wan, Z. (2006). Satellite-derived, melt-season surface temperature of the Greenland Ice Sheet (2000-2005) and its relationship to mass balance. *Geophysical Research Letters*, 33:L11501, doi:10.1029/2006GL026444

Hall, D.K., Williams, R.S., Luthcke, S.B., & Digirolamo, N.E. (2008). Greenland ice sheet surface temperature, melt and mass loss: 2000-06. *Journal of Glaciology*, 54, 81-93

Hook, S., Johnson, W., & Abrams, M. (2013). NASA's Hyperspectral Thermal Emission Spectrometer (HyTES). In C. Kuenzer, & S. Dech (Eds.), *Thermal Infrared Remote Sensing - Sensors, Methods, Applications*: Springer

Hook, S.J., Dmochowski, J.E., Howard, K.A., Rowan, L.C., Karlstrom, K.E., & Stock, J.M. (2005). Mapping variations in weight percent silica measured from multispectral thermal infrared imagery - Examples from the Hiller Mountains, Nevada, USA and Tres Virgenes-La Reforma, Baja California Sur, Mexico. *Remote Sensing of Environment*, 95, 273-289

Hook, S.J., Vaughan, R.G., Tonooka, H., & Schladow, S.G. (2007). Absolute radiometric in-flight validation of mid infrared and thermal infrared data from ASTER and MODIS on the terra spacecraft using the Lake Tahoe, CA/NV, USA, automated validation site. *Ieee Transactions on Geoscience and Remote Sensing*, 45, 1798-1807

Hulley, G., Hook, S., & Hughes, C. (2012). MODIS MOD21 Land Surface Temperature and Emissivity Algorithm Theoretical Basis Document. In: Jet Propulsion Laboratory, California Institute of Technology, JPL Publication 12-17, August, 2012

Hulley, G.C., & Hook, S.J. (2009a). Intercomparison of Versions 4, 4.1 and 5 of the MODIS Land Surface Temperature and Emissivity Products and Validation with Laboratory Measurements of Sand Samples from the Namib Desert, Namibia. *Remote Sensing of Environment*, *113*, 1313-1318

Hulley, G.C., & Hook, S.J. (2009b). The North American ASTER Land Surface Emissivity Database (NAALSED) Version 2.0. *Remote Sensing of Environment*, *113*, 1967-1975

Hulley, G.C., Hook, S.J., Abbott, E., Malakar, N., Islam, T., & Abrams, M. (2015). The ASTER Global Emissivity Dataset (ASTER GED): Mapping Earth's emissivity at 100 meter spatial scale. *Geophysical Research Letters*, *42*, 7966-7976

Hulley, G.C., Hook, S.J., & Baldrige, A.M. (2008). ASTER land surface emissivity database of California and Nevada. *Geophysical Research Letters*, *35*, L13401, doi: 10.1029/2008gl034507

Hulley, G.C., Hook, S.J., & Baldrige, A.M. (2009a). Validation of the North American ASTER Land Surface Emissivity Database (NAALSED) Version 2.0 using Pseudo-Invariant Sand Dune Sites. *Remote Sensing of Environment*, *113*, 2224-2233

Hulley, G.C., Hook, S.J., & Baldrige, A.M. (2010). Investigating the Effects of Soil Moisture on Thermal Infrared Land Surface Temperature and Emissivity Using Satellite Retrievals and Laboratory Measurements. *Remote Sensing of Environment*, *114*, 1480-1493

Hulley, G.C., Hook, S.J., Manning, E., Lee, S.Y., & Fetzer, E.J. (2009b). Validation of the Atmospheric Infrared Sounder (AIRS) Version 5 (v5) Land Surface Emissivity Product over the Namib and Kalahari Deserts. *Journal of Geophysical Research Atmospheres*, *114*, D19104

Jin, M.L., & Liang, S.L. (2006). An improved land surface emissivity parameter for land surface models using global remote sensing observations. *Journal of Climate*, *19*, 2867-2881

Justice, C., & Townshend, J. (2002). Special issue on the moderate resolution imaging spectroradiometer (MODIS): a new generation of land surface monitoring. *Remote Sensing of Environment*, *83*, 1-2

Kalnay, E., Kanamitsu, M., & Baker, W.E. (1990). Global Numerical Weather Prediction at the National-Meteorological-Center. *Bulletin of the American Meteorological Society*, *71*, 1410-1428

Kealy, P.S., & Hook, S. (1993). Separating temperature & emissivity in thermal infrared multispectral scanner data: Implication for recovering land surface temperatures. *IEEE Transactions on Geoscience and Remote Sensing*, *31*, 1155-1164

Kinter, J.L., Shukla, J., Marx, L., & Schneider, E.K. (1988). A simulation of the winter and summer circulations with the NMC global spectral model. *Journal of Atmospheric Science*, *45*, 2486-2522

Li, Z.L., Becker, F., Stoll, M.P., & Wan, Z.M. (1999). Evaluation of six methods for extracting relative emissivity spectra from thermal infrared images. *Remote Sensing of Environment*, *69*, 197-214

Lyon, R. (1965). Analysis of ROcks by Spectral INfrared Emission (8 to 25 microns). *Economic Geology and the Bulletin of the Society of Economic Geologists*, *60*, 715-736

Matricardi, M. (2008). The generation of RTTOV regression coefficients for IASI and AIRS using a new profile training set and a new line-by-line database. In: ECMWF Research Dept. Tech. Memo.

Matricardi, M. (2009). Technical Note: An assessment of the accuracy of the RTTOV fast radiative transfer model using IASI data. *Atmospheric Chemistry and Physics*, 9, 6899-6913

Matricardi, M., Chevallier, F., & Tjemkes, S.A. (2001). An improved general fast radiative transfer model for the assimilation of radiance observations. In: European Centre for Medium-Range Weather Forecasts

Matricardi, M., & Saunders, R. (1999). Fast radiative transfer model for simulation of infrared atmospheric sounding interferometer radiances. *Applied Optics*, 38, 5679-5691

Matsunaga, T. (1994). A temperature-emissivity separation method using an empirical relationship between the mean, the maximum, & the minimum of the thermal infrared emissivity spectrum, in Japanese with English abstract. *Journal Remote Sensing Society Japan*, 14, 230-241

Merchant, C.J. (2012). The Surface Temperatures of the Earth: Steps towards Integrated Understanding of Variability and Change. *EarthTemp network meeting, Edinburgh, 25-27 June, 2012*, [www.earthtemp.net](http://www.earthtemp.net)

Mira, M., Valor, E., Boluda, R., Caselles, V., & Coll, C. (2007). Influence of soil water content on the thermal infrared emissivity of bare soils: Implication for land surface temperature determination. *Journal of Geophysical Research-Earth Surface*, 112, F04003

Moran, M.S. (2003). Thermal infrared measurement as an indicator of plant ecosystem health, in: *Thermal Remote Sensing in Land Surface Processes*, edited: Quattrochi, D. A. and Luvall, J., Taylor and Francis, 257-282

Mushkin, A., & Gillespie, A.R. (2005). Estimating sub-pixel surface roughness using remotely sensed stereoscopic data. *Remote Sensing of Environment*, 99, 75-83

Norman, J.M., & Becker, F. (1995). Terminology in Thermal Infrared Remote-Sensing of Natural Surfaces. *Agricultural and Forest Meteorology*, 77, 153-166

Ogawa, K. (2004). Mapping Surface Broadband Emissivity of the Sahara Desert Using ASTER and MODIS Data. *Earth Interactions*, 8, -

Ogawa, K., Schmugge, T., Jacob, F., & French, A. (2003). Estimation of land surface window (8-12  $\mu$  m) emissivity from multispectral thermal infrared remote sensing - A case study in a part of Sahara Desert. *Geophysical Research Letters*, 30, -

Ogawa, K., Schmugge, T., & Rokugawa, S. (2006). Observations of the dependence of the thermal infrared emissivity on soil moisture. *Geophysical Research Abstracts*, 8, 04996

Oleson, K.W., Bonan, G.B., Levis, S., & Vertenstein, M. (2004). Effects of land use change on North American climate: impact of surface datasets and model biogeophysics. *Climate Dynamics*, 23, 117-132

Palluconi, F., Hoover, G., Alley, R.E., Nilsen, M.J., & Thompson, T. (1999). An atmospheric correction method for ASTER thermal radiometry over land, ASTER algorithm theoretical basis document (ATBD), Revision 3, Jet Propulsion Laboratory, Pasadena, CA, 1999

Parkinson, C.L., Cavalieri, D.J., Gloersen, P., Zwally, H.J., & Comiso, J.C. (1999). Arctic sea ice extents, areas, and trends, 1978-1996. *Journal of Geophysical Research-Oceans*, 104, 20837-20856

Rhee, J., Im, J., & Carbone, G.J. (2010). Monitoring agricultural drought for arid and humid regions using multi-sensor remote sensing data. *Remote Sensing of Environment*, 114, 2875-2887

Saunders, R., Matricardi, M., & Brunel, P. (1999). An improved fast radiative transfer model for assimilation of satellite radiance observations. *Quarterly Journal of the Royal Meteorological Society*, 125, 1407-1425

- Seemann, S.W., Li, J., Menzel, W.P., & Gumley, L.E. (2003). Operational retrieval of atmospheric temperature, moisture, and ozone from MODIS infrared radiances. *Journal of Applied Meteorology*, 42, 1072-1091
- Snyder, W.C., Wan, Z., Zhang, Y., & Feng, Y.Z. (1998). Classification-based emissivity for land surface temperature measurement from space. *International Journal of Remote Sensing*, 19, 2753-2774
- Susskind, J., Barnet, C.D., & Blaisdell, J.M. (2003). Retrieval of atmospheric and surface parameters from AIRS/AMSU/HSB data in the presence of clouds. *IEEE Transactions on Geoscience and Remote Sensing*, 41, 390-409
- Teillet, P.M., Fedosejevs, G., Gautier, R.P., & Schowengerdt, R.A. (1998). Uniformity characterization of land test sites used for radiometric calibration of earth observation sensors. In, *Proc. 20th Can. Symp. Remote Sensing* (pp. 1-4). Calgary, AB, Canada
- Tonooka, H. (2005). Accurate atmospheric correction of ASTER thermal infrared imagery using the WVS method. *Ieee Transactions on Geoscience and Remote Sensing*, 43, 2778-2792
- Tonooka, H., & Palluconi, F.D. (2005). Validation of ASTER/TIR standard atmospheric correction using water surfaces. *Ieee Transactions on Geoscience and Remote Sensing*, 43, 2769-2777
- Vaughan, R.G., Hook, S.J., Calvin, W.M., & Taranik, J.V. (2005). Surface mineral mapping at Steamboat Springs, Nevada, USA, with multi-wavelength thermal infrared images. *Remote Sensing of Environment*, 99, 140-158
- Wan, Z., & Li, Z.L. (2008). Radiance-based validation of the V5 MODIS land-surface temperature product. *International Journal of Remote Sensing*, 29, 5373-5395
- Wan, Z., Zhang, Y., Zhang, Q., & Li, Z.L. (2004). Quality assessment and validation of the MODIS global land surface temperature. *International Journal of Remote Sensing*, 25, 261-274
- Wan, Z.M. (2008). New refinements and validation of the MODIS Land-Surface Temperature/Emissivity products. *Remote Sensing of Environment*, 112, 59-74
- Wang, K.C., & Liang, S.L. (2009). Evaluation of ASTER and MODIS land surface temperature and emissivity products using long-term surface longwave radiation observations at SURFRAD sites. *Remote Sensing of Environment*, 113, 1556-1565
- Yao, Z.G., Li, J., Li, J.L., & Zhang, H. (2011). Surface Emissivity Impact on Temperature and Moisture Soundings from Hyperspectral Infrared Radiance Measurements. *Journal of Applied Meteorology and Climatology*, 50, 1225-1235
- Zeng, Q.C., Zhang, X.H., Liang, X.Z., Yuan, C.G., & Chen, S.F. (1989). Documentation of IAP two-level atmospheric general circulation model. In U.S.D.o. Energy (Ed.) (p. 383 pp.). Washington, D.C.
- Zhou, L., Dickinson, R.E., Ogawa, K., Tian, Y., Jin, M., Schmugge, T., & Tsvetsinskaya, E. (2003a). Relations between albedos and emissivities from MODIS and ASTER data over North African desert. *Geophysical Research Letters*, 30, -
- Zhou, L., Dickinson, R.E., Tian, Y., Jin, M., Ogawa, K., Yu, H., & Schmugge, T. (2003b). A sensitivity study of climate and energy balance simulations with use of satellite-derived emissivity data over Northern Africa and the Arabian Peninsula. *Journal of Geophysical Research-Atmospheres*, 108, 4795